

NASA TECHNICAL MEMORANDUM

NASA TM X-73374

(NASA-TM-X-73374) MINIATURIZED POINTING
MOUNT PERFORMANCE ANALYSIS (NASA) 51 p HC
A04/MF A01 CSCL 14B

N77-20403

Unclas
21744

G3/35

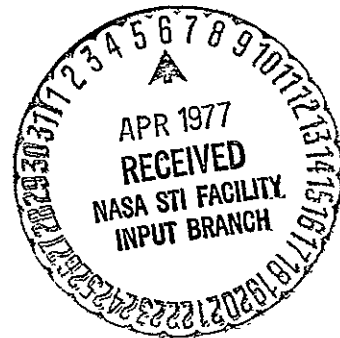
MINIATURIZED POINTING MOUNT PERFORMANCE ANALYSIS

By Joe T. Howell, Jr.
Program Development

November 1976

NASA

*Jo
GS to ND*



*George C. Marshall Space Flight Center
Marshall Space Flight Center, Alabama*

TABLE OF CONTENTS

	Page
INTRODUCTION	1
INERTIAL POINTING PERFORMANCE	2
SLEWING AND TRACKING PERFORMANCE	12
Slewing	12
Tracking	16
RASTERING PERFORMANCE	19
CONCLUSION	33
APPENDIX A — SIMULATION MATH MODEL	35
APPENDIX B — MINIMUM TIME RASTER SCAN	38
REFERENCES	42
BIBLIOGRAPHY	42

LIST OF ILLUSTRATIONS

Figure	Title	Page
1.	Simulation model	2
2.	Man motion design profile	3
3.	System flow diagram	5
4.	MPM pointing performance for 130 kg instrument	6
5.	MPM pointing performance for 500 kg instrument	7
6.	MPM performance for 130 kg instrument at different control frequencies	8
7.	MPM performance for 500 kg instrument at different control frequencies	9
8.	MPM stability for various instrument sizes	10
9.	MPM stability rate for various instrument sizes	11
10.	Slew command profiles	12
11.	MPM slewing performance	13
12.	MPM torque limit for slew maneuvers	14
13.	MPM isolator limit for slew maneuvers	15
14.	Rigid end mount slewing analysis	16
15.	Rigid end mount slewing capability for 0.6 Nm torque limit	17
16.	Rigid c.g. mount slewing capability for 0.6 Nm torque limit	18

LIST OF ILLUSTRATIONS (Concluded)

Figure	Title	Page
17.	MPM tracking performance	19
18.	Raster scanning a region	20
19.	Raster scan command profile	22
20.	MPM rastering torque versus scan rate for the 90 arc s raster	24
21.	End mount/c.g. mount control torque ratio for a simplified end mount model	26
22.	MPM rastering torque versus shockmount stiffness for the 90 arc s raster	27
23.	MPM rastering torque versus shockmount stiffness for the 3600 arc s raster	28
24.	MPM rastering torque versus pedestal height for the 90 arc s raster	29
25.	Typical rastering dynamic response	30
26.	Scan line transition command profile	31
27.	Typical MPM response to scan line transition	32

LIST OF TABLES

Table	Title	Page
1.	Summary of Nominal Mass Characteristics	3
2.	Summary of Nominal MPM Characteristics	4
3.	MPM and Instrument Characteristics for Rastering	21
4.	Nominal Rastering Requirements	21
5.	MPM Rastering Performance	23

LIST OF SYMBOLS

<u>Symbol</u>	<u>Definition</u>
D_R	Rotational spring damping
D_T	Translational spring damping
F_M	Man motion disturbance force
I_S	Shuttle moment of inertia
I_1	Instrument with inner gimbal moment of inertia
K_I	Integral control gain
K_P	Position control gain
K_R	Rotational spring stiffness
K_T	Translational spring stiffness
K_1	Rate control gain
M_S	Shuttle mass
M_1	Instrument with inner gimbal mass
R_M	Location of the man motion disturbance forward of the Shuttle c. m.
R_1	Instrument c. m. offset
R_2	Pedestal height
R_3	Location of the pedestal suspension aft of the Shuttle c. m.
T_C	Instrument control torque

LIST OF SYMBOLS (Concluded)

<u>Symbol</u>	<u>Definition</u>
X_S	Translation of the Shuttle c.m. in the X direction
X_1	Translation of the instrument with inner gimbal c.m. in the X direction
Z_S	Translation of the Shuttle c.m. in the Z direction
Z_1	Translation of the instrument with inner gimbal c.m. in the Z direction
θ_C	Instrument line of sight command angle or pointing position command
θ_E	Instrument line of sight error angle
θ_S	Inertial angle of the Shuttle
θ_1	Inertial angle of the instrument
θ_2	Inertial angle of the pedestal

MINIATURIZED POINTING MOUNT PERFORMANCE ANALYSIS

INTRODUCTION

The Miniaturized Pointing Mount (MPM) has been proposed as a lightweight low cost pointing mount to satisfy the pointing requirements of small instruments, especially for the early Spacelab missions and Orbital Flight Test (OFT) missions which precede Spacelab. Reference 1 defines small instrument requirements and Reference 2 describes the MPM, associated subsystems, computer simulations, and general philosophy. For completeness, some of the simulation results from Reference 2 will be repeated in this report.

MPM performance is investigated using a planar model of the pointing system as depicted in Figure 1. The model represents 2 degrees of translation and 1 degree of rotation for each of the three bodies (i.e., the instrument, pedestal, and Shuttle). The investigation consisted primarily of computer simulation analyses of MPM dynamics with some analytical calculations of specific cases. The performance includes inertial pointing, slewing, tracking, and rastering.

MPM inertial pointing performance with man motion disturbance is given for two typical instruments as well as for instrument parameter variations. MPM sensitivity to pointing position and control frequency is also shown.

MPM slewing performance (i.e., for changing targets) is given for two typical instruments and for instrument parameter variations. For comparison, analytical analyses of a rigid end mount and a rigid c.g. mount are shown.

Tracking of an Earth surface target is demonstrated for two typical instruments. MPM performance is given as peak control torque required as a function of orbital altitude or peak tracking rate.

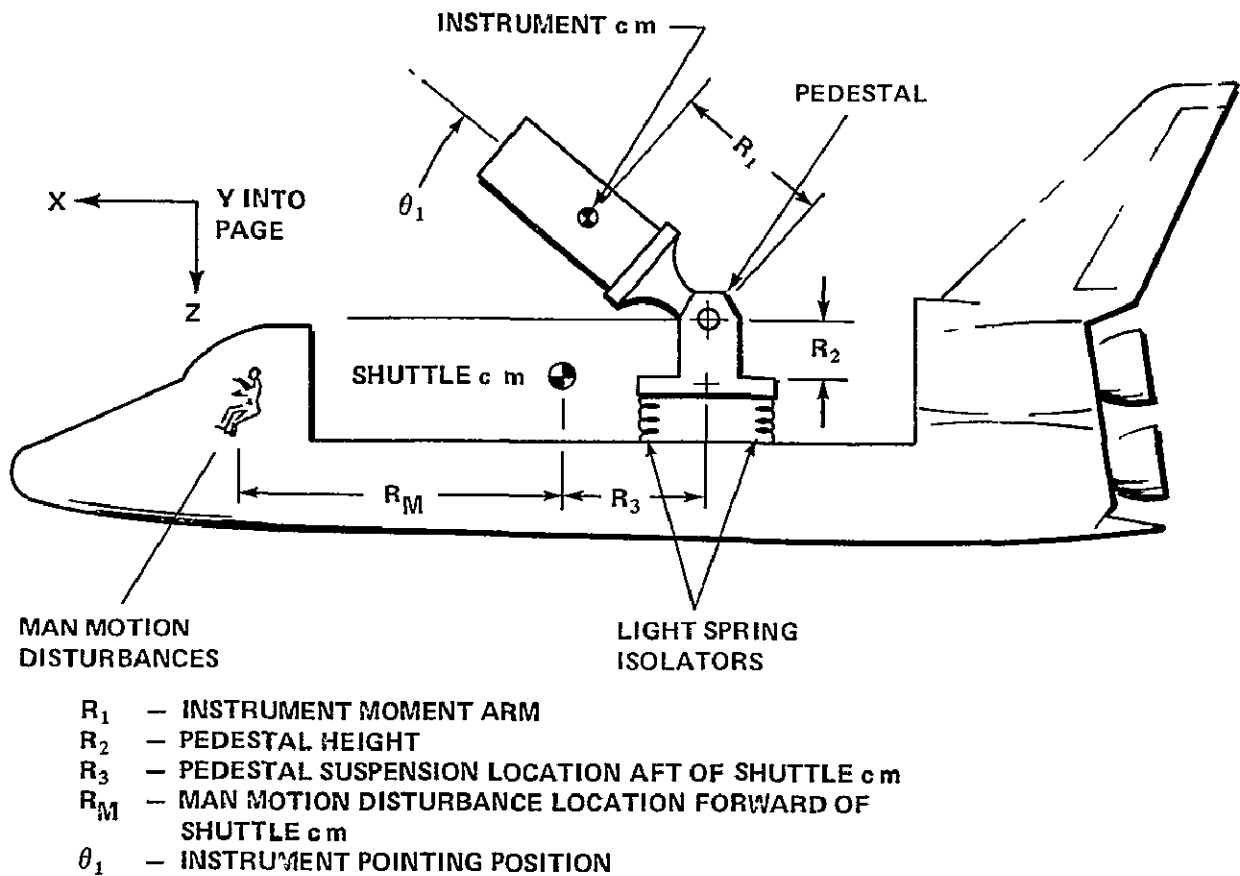


Figure 1. Simulation model.

MPM raster scanning or simply rastering performance of a typical instrument is presented for typical rastering requirements and for variations of scan rate, pointing position, shockmount stiffness, and pedestal height.

INERTIAL POINTING PERFORMANCE

Inertial pointing refers to solar and stellar type observations where the target line of sight is essentially fixed in space and usually places the most severe stability requirement on the pointing system. Therefore, MPM performance is given for the predominant disturbance which is the result of man motion as determined from Skylab experience [3]. The man motion disturbance

profile depicted in Figure 2 was recommended in Reference 1 as a design profile for crew motion and has been used extensively in instrument pointing systems analysis. The profile in Figure 2 was used to impart a 40 Ns impulse on the Shuttle at the crew station approximately 15 m forward of the Shuttle c.g. A summary of the nominal mass characteristics is shown in Table 1, and a summary of nominal MPM characteristics is shown in Table 2.

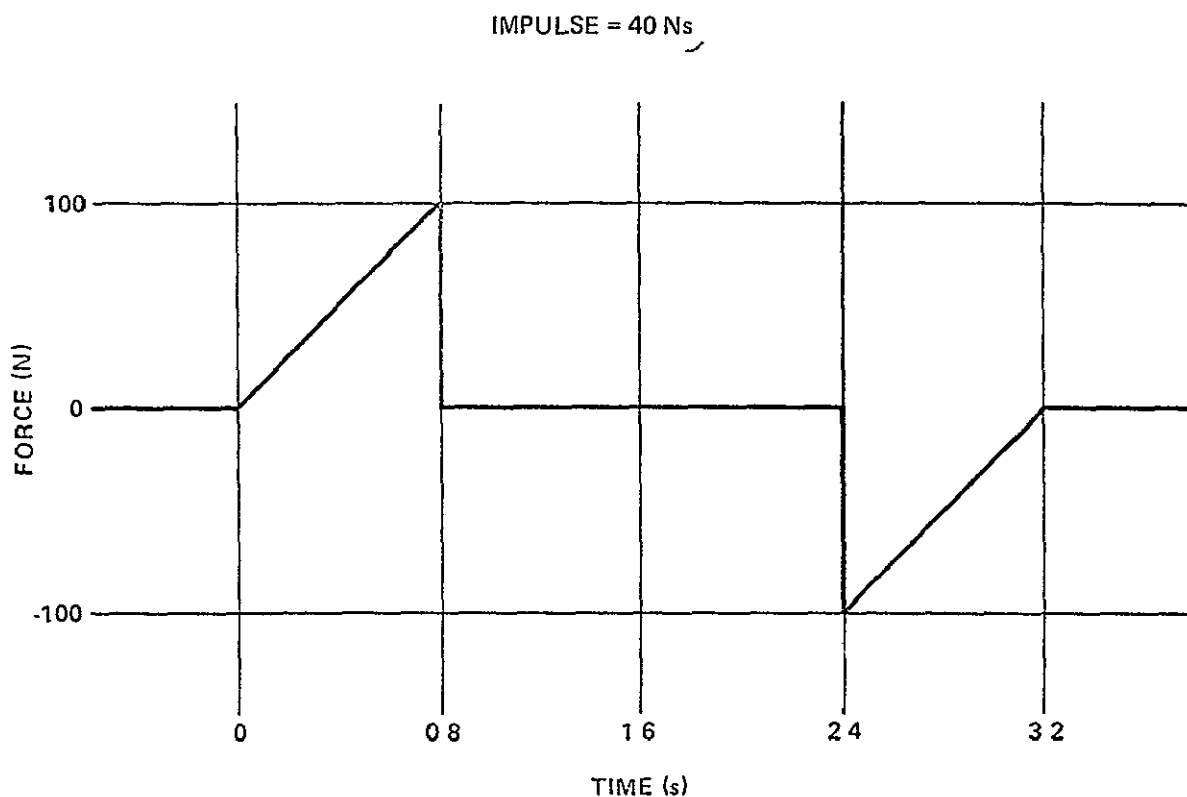


Figure 2. Man motion design profile.

TABLE 1. SUMMARY OF NOMINAL MASS CHARACTERISTICS

Item	Mass (kg)	Inertia (kg m ²)
Shuttle/Pallet	71 420	7 215 000
MPM Pedestal	23.4	2.34
Experiment Package		
Small	130	52
Large	500	500

TABLE 2. SUMMARY OF NOMINAL MPM CHARACTERISTICS

Shockmount Stiffness (N/m)	
Soft Mounted	100 and 250
Hard Mounted	10^5
Instrument Moment Arm (m)	1.0
Pedestal Height (m)	0.44
Control Loop Bandwidth (Hz)	
Soft Mounted Inertial Pointing	3
Hard Mounted Inertial Pointing	0.5
Earth Surface Target Tracking	5

The system flow diagram shown in Figure 3 depicts the dynamic interaction between the three bodies. The man motion disturbances on the Shuttle are partially attenuated by soft isolators. However, a most important function of the isolators to fine pointing is the freedom of the experiment to float relative to the Shuttle. The gimbal translates with the experiment while maintaining the desired pointing attitude. Structural stiffness or gimbal compliance of the gimbal shaft was included between the pedestal and the experiment. The experiment control law has position plus rate feedback with the option of adding the integral of position feedback for tracking or slew maneuvers.

Two different mathematical models were derived and used to simulate the dynamic response of the MPM. One model was presented in Appendix B of Reference 2, and the other model is presented in Appendix A of this report. Both models were programmed on analog and digital computers. The analog simulations were used to probe the overall system and determine nominal control gains and isolator characteristics. The digital simulations were used to verify the analog results and to vary parameters that were inconvenient to vary in the analog simulation because of amplitude scaling considerations.

The computer outputs were primarily chart recordings; however, they have been processed for quick and easy interpretation. The stability and control torque are shown in Figure 4 as a function of the pointing position for the small

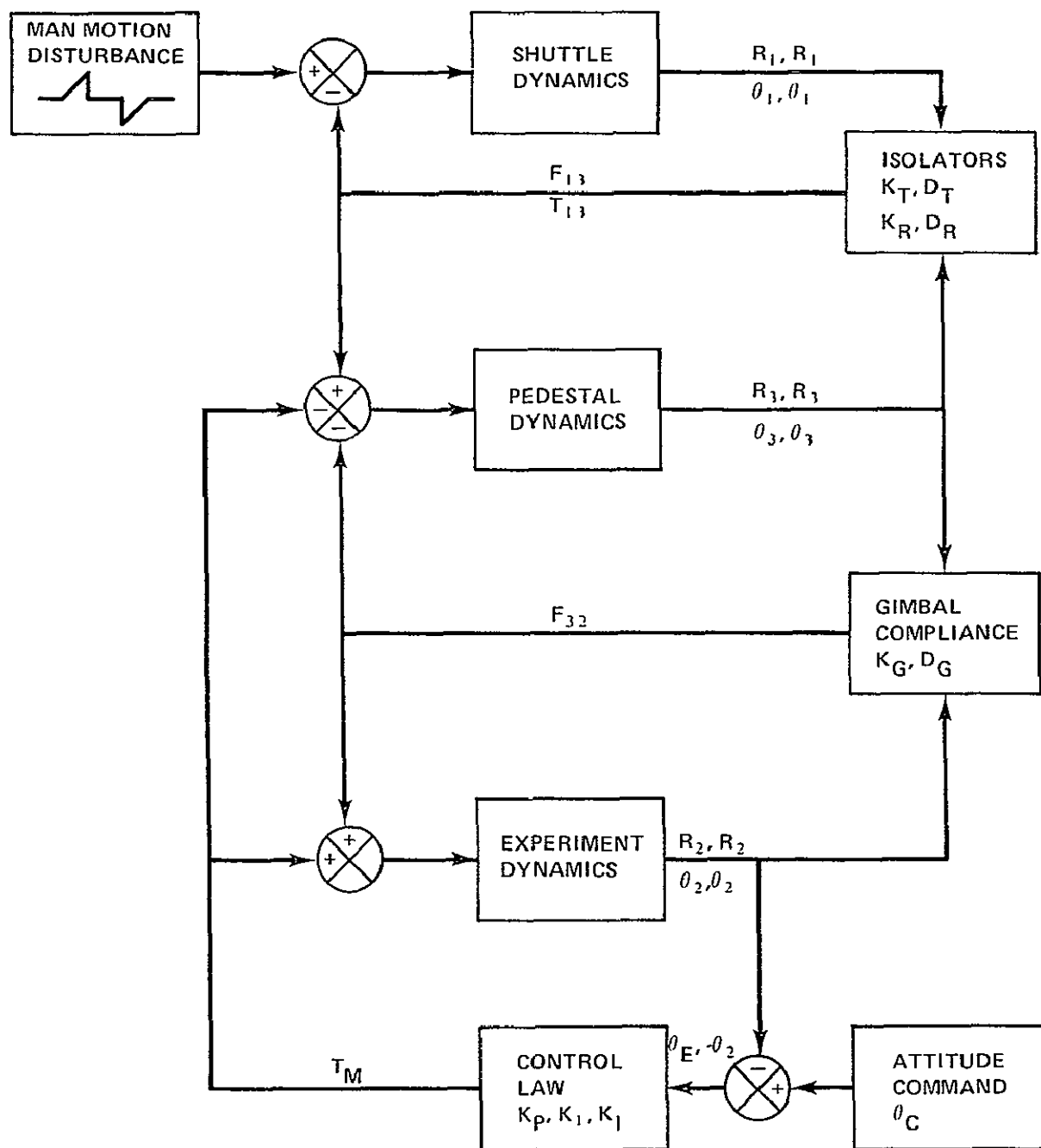


Figure 3. System flow diagram.

PEAK STABILITY ERROR AND PEAK CONTROL TORQUE VERSUS POINTING POSITION FOR 130 kg INSTRUMENT (SCHWARZSCHILD) WITH SHUTTLE MAN MOTION DISTURBANCE
 NO FRICTION OR CABLE TORQUE
 NO SENSOR NOISE OR DRIFT

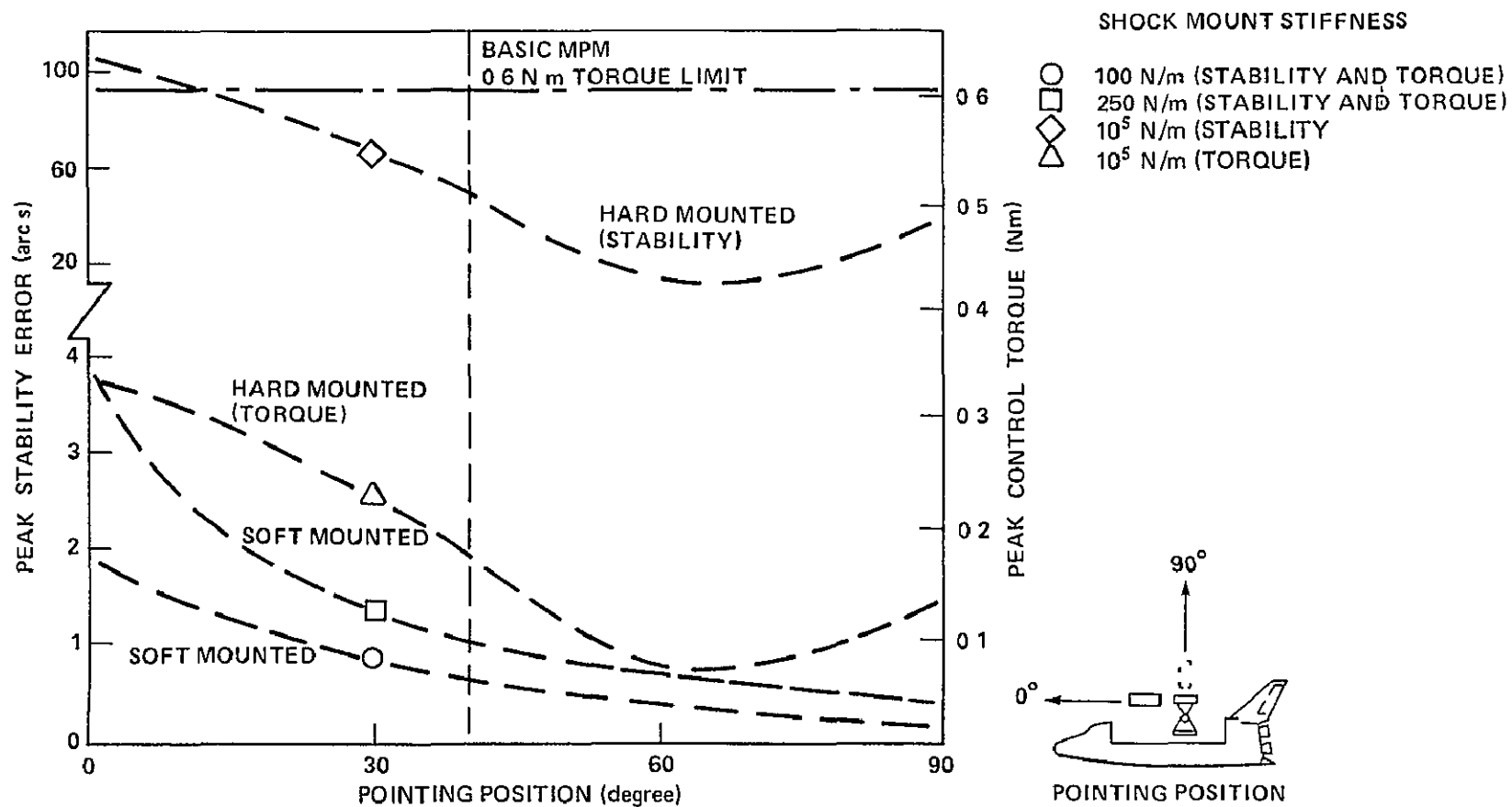


Figure 4. MPM pointing performance for 130 kg instrument.

payload with man motion disturbance on the Shuttle. Similar information is given in Figure 5 for the large payload. The system parameters associated with Figures 4 and 5 are shown in Tables 1 and 2. Particular attention should be focused on pointing position and instrument weight. The most favorable pointing position appears to be in the 40 to 90 degree range. The large instrument shows much better pointing stability for the same disturbance and system parameters; however, the small instrument requires much less control torque.

To determine MPM sensitivity to a variation in control frequency, the basic controller frequency was varied over a range of 1 to 5 Hz. The stability and control torques are presented in Figures 6 and 7 for the small and large instruments. It is interesting to note the decrease in stability error for an increase in controller frequency, while the control torque remains the same for each frequency.

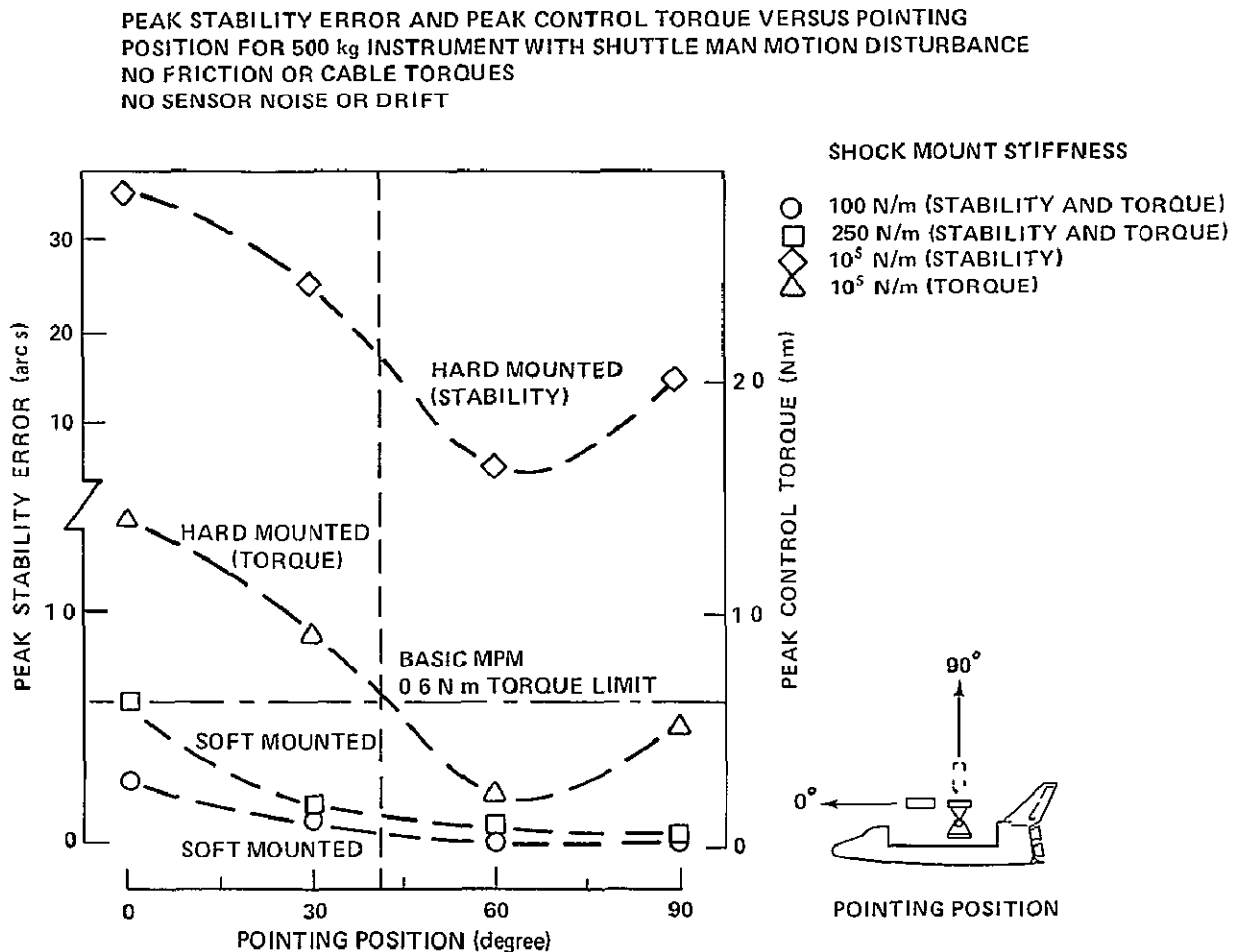


Figure 5. MPM pointing performance for 500 kg instrument.

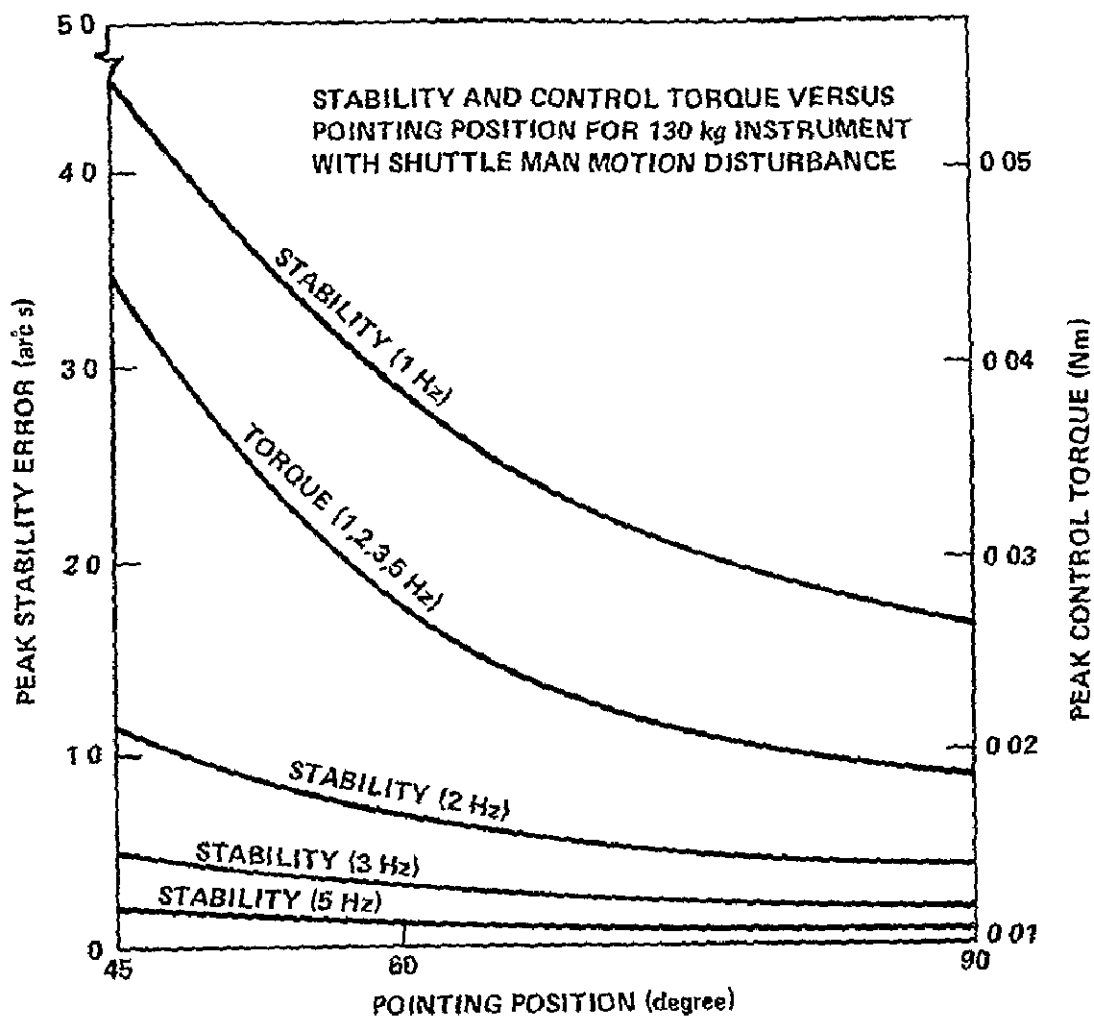


Figure 6. MPM performance for 130 kg instrument at different control frequencies.

Instrument length, diameter, and mass were varied to show MPM sensitivity to instrument shape and mass characteristics. The MPM control frequency was varied linearly as a function of inertia such that the control frequency was approximately 5 Hz for small instruments (e.g., 10 to 100 kg m²) and 2 Hz for large instruments (e.g., 5000 kg m²). Figures 8 and 9 show the general trend for stability and stability rate, respectively, to the variation in instrument characteristics. For the smaller type instrument with an inertia less than 100 kg m², the two separate curves represent the contrasting instrument shapes. The upper curve represents the short, flat type instruments whereas the lower curve characterizes the long, slim type instruments. For the larger instrument with an inertia greater than 100 kg m², the MPM appears to be insensitive to instrument shape.

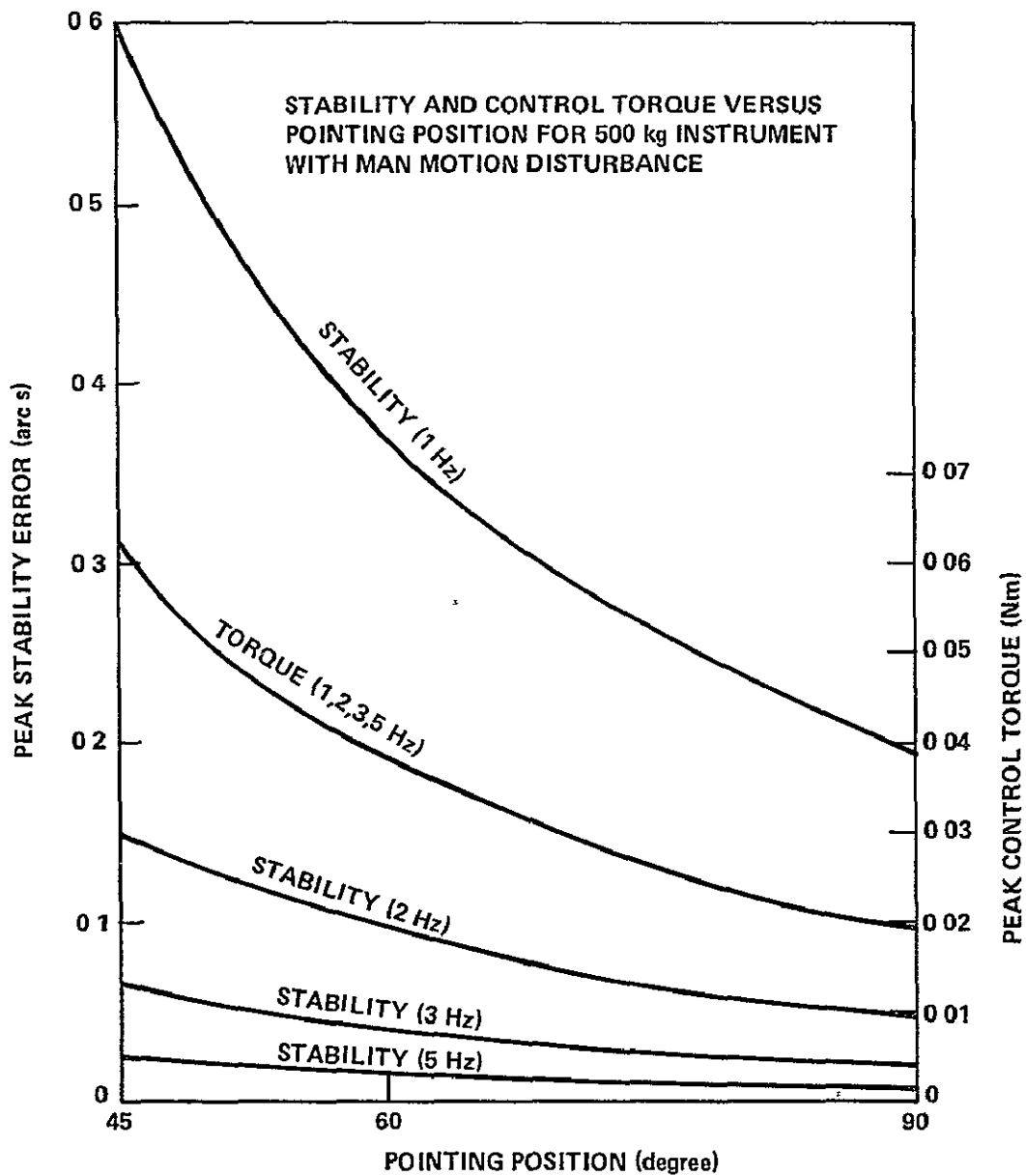


Figure 7. MPM performance for 500 kg instrument at different control frequencies.

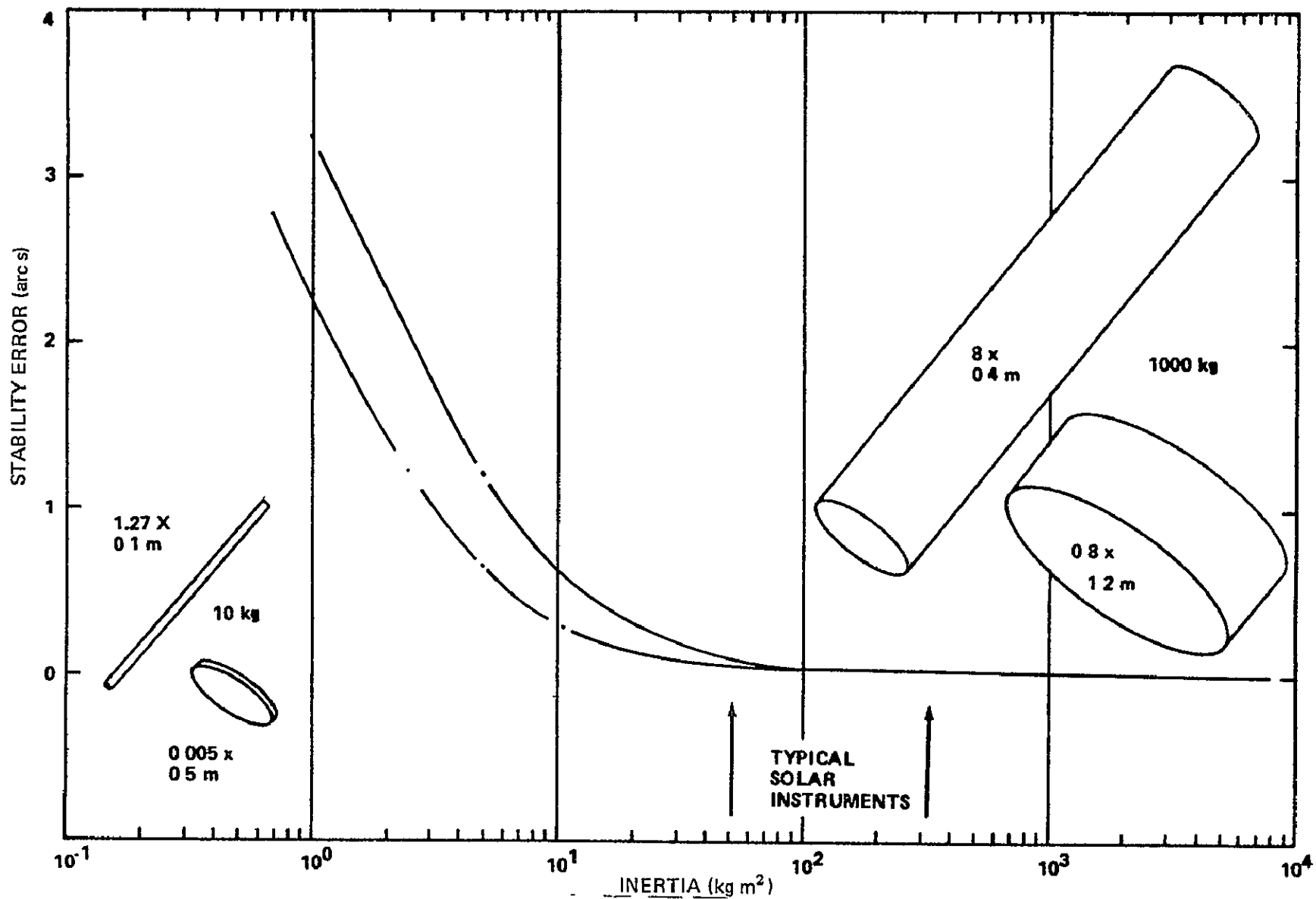


Figure 8. MPM stability for various instrument sizes.

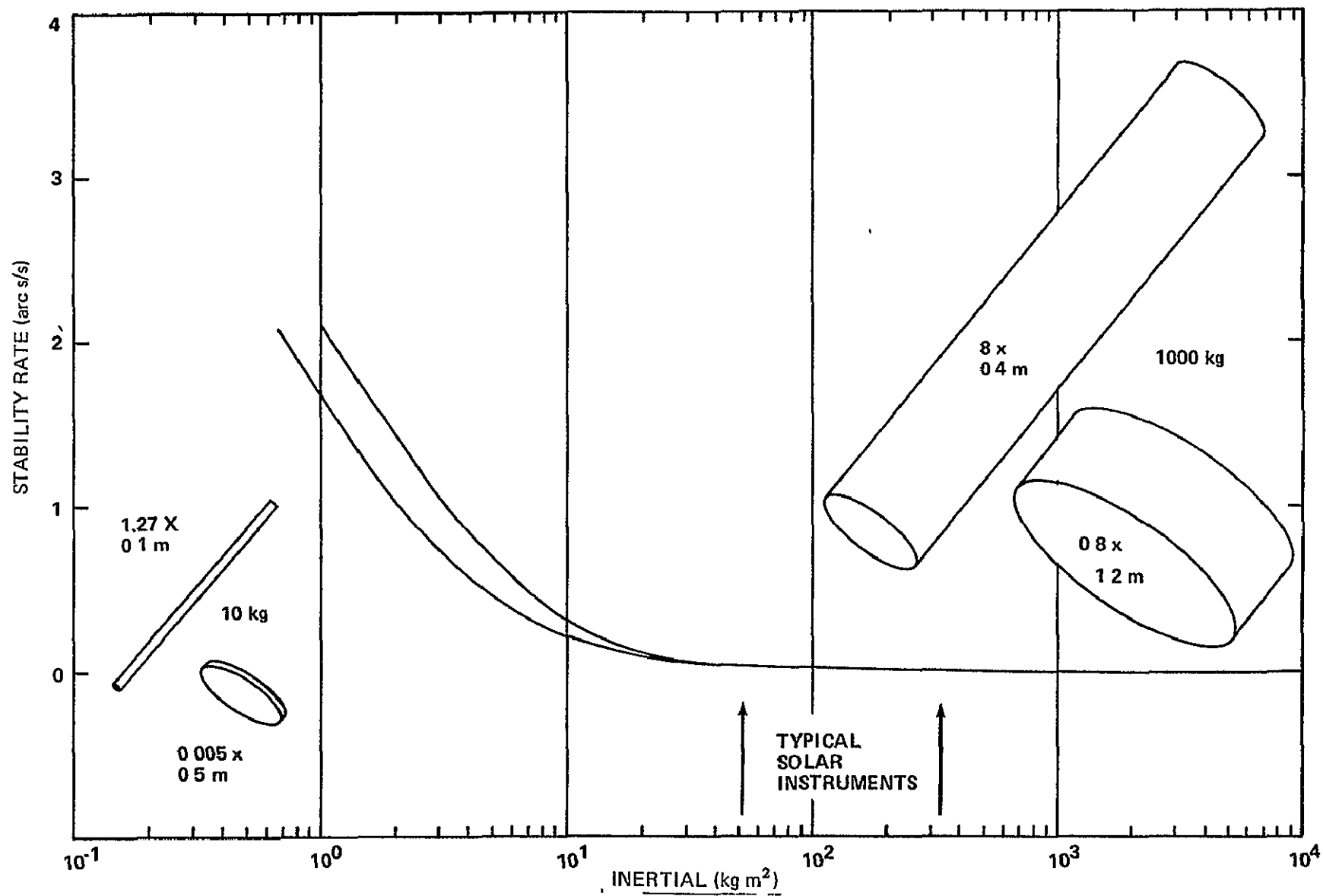


Figure 9. MPM stability rate for various instrument sizes.

SLEWING AND TRACKING PERFORMANCE

Slewing and tracking performance is presented for the small and large instruments using nominal system parameters. Slewing control torque and isolator extension are also given for an instrument parameter variation. Slewing analysis of a rigid c.g. mount is also presented for comparison.

Slewing

Changing targets or slewing requires knowledge of both the pointing system capability and the relative locations of the targets to the pointing system. The slew angle is dictated by the target locations, but the slewing period or peak slewing rate can be selected to stay within the system torque capability. Figure 10 shows the type slew profiles used in this study. Typical MPM slewing performance is given in Figure 11 for the small and large instruments. The large instrument requires up to 150 s to slew 90 degrees whereas the small instrument can slew 90 degrees in less than 100 s and still be within the basic MPM torque capability of 0.6 Nm. The slew maneuver control law was designed to track the command profile with a 1 arc s steady-state error using position, rate, and integral of position feedback.

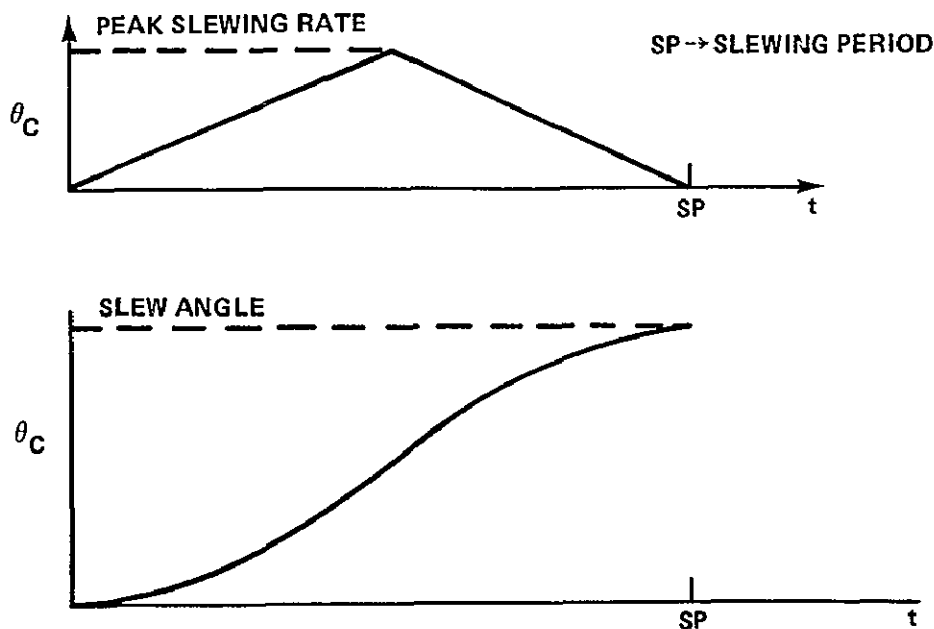


Figure 10. Slew command profiles.

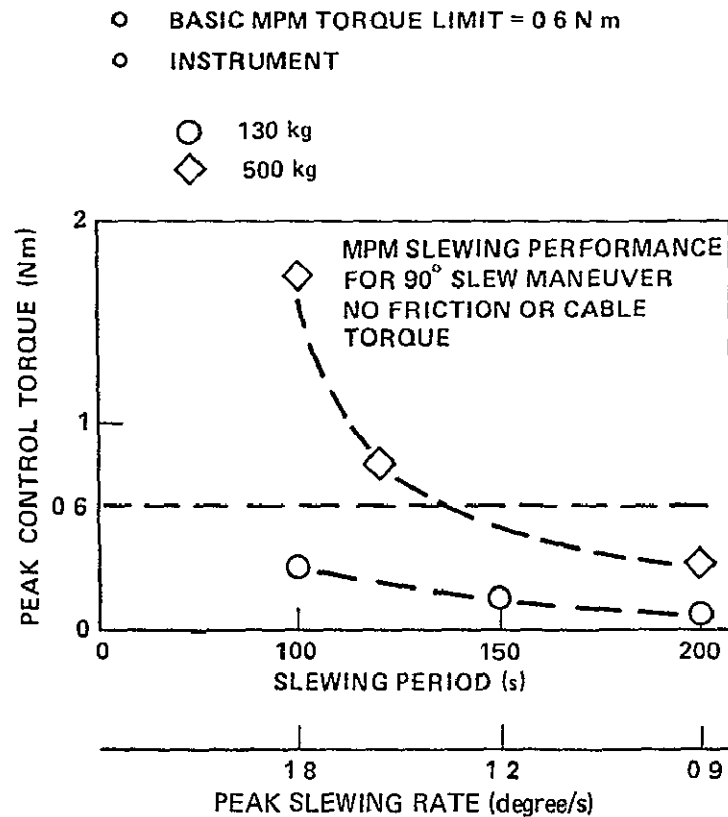


Figure 11. MPM slewing performance.

An instrument parameter variation was made for a 90 degree slew maneuver for 100 and 200 s slewing periods. Figure 12 shows the general trend of control torque required as a function of instrument inertia and slewing period while Figure 13 shows the general trend of isolator extension. This demonstrates the practical limits of using MPM with soft isolators for slewing. Within the same volume limit of the existing torquer motor, the MPM torque capability could be upgraded to approximately 1.2 Nm.

The torque required to perform slew maneuvers with a rigid end mount was determined analytically assuming the slew command profile of Figure 10. A rigid end mount is used to denote MPM isolators in the caged position or the pedestal mounted directly to the Shuttle/pallet without isolators. Figure 14 gives the slewing torque required to perform a 90 degree slew maneuver as a function of slewing period for the small and large instruments. The torque required to slew 90 degrees is approximately three times greater for the MPM with 100 N/m isolators than for a rigid end mount as can be seen by comparing Figures 11 and 14. This demonstrates the effect of the translational/rotational coupling due

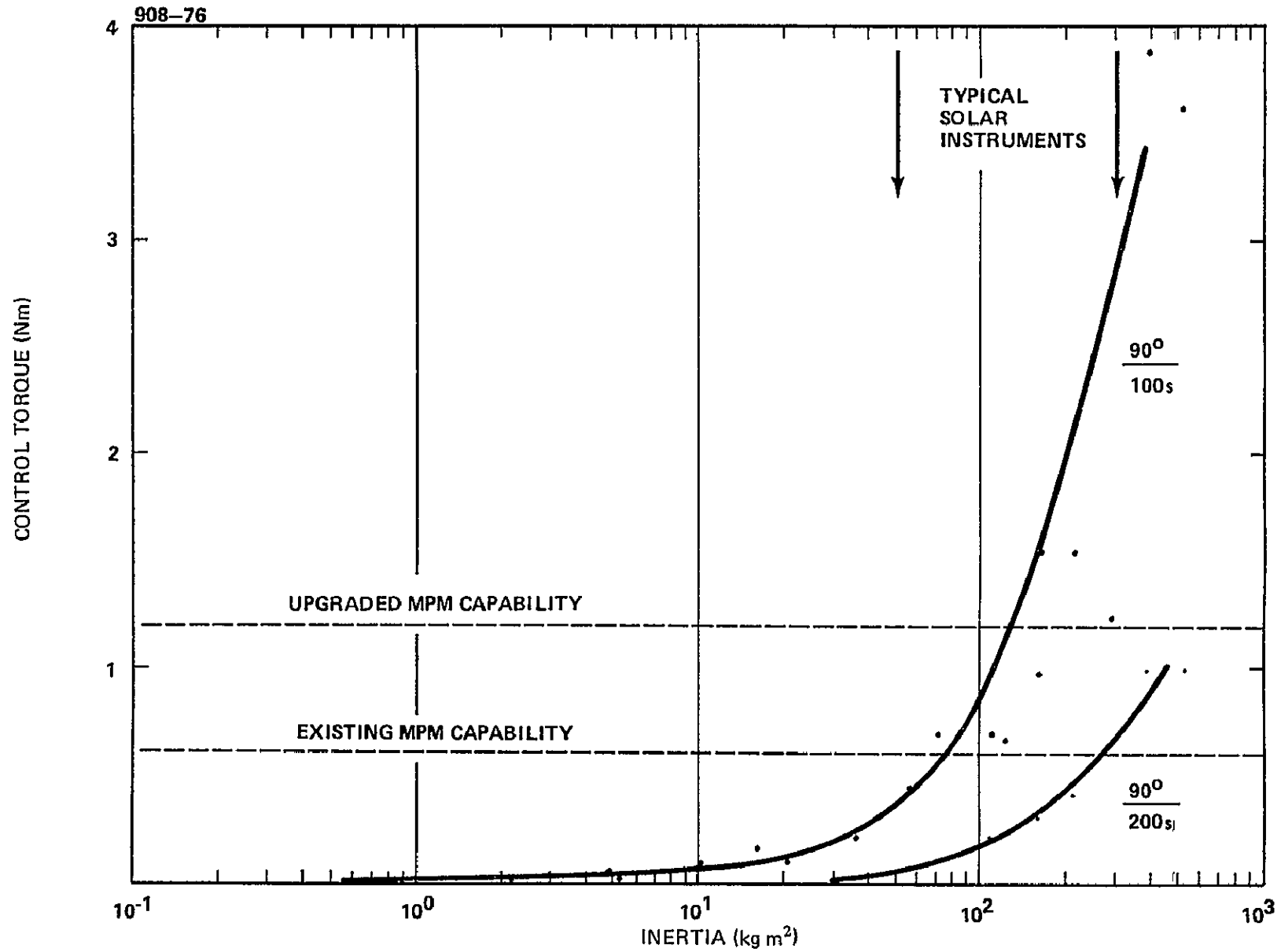


Figure 12. MPM torque limit for slew maneuvers.

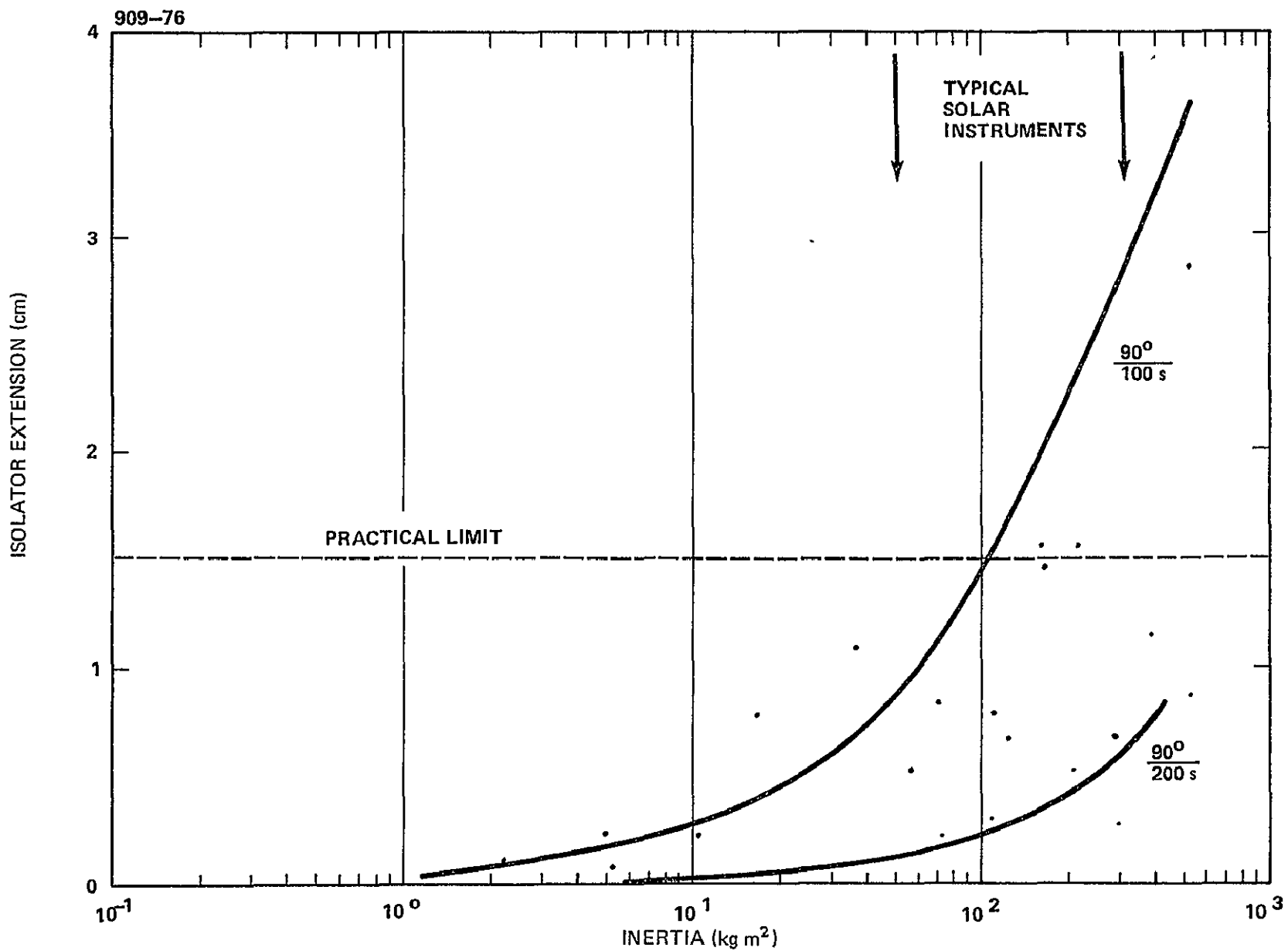


Figure 13. MPM isolator limit for slew maneuvers.

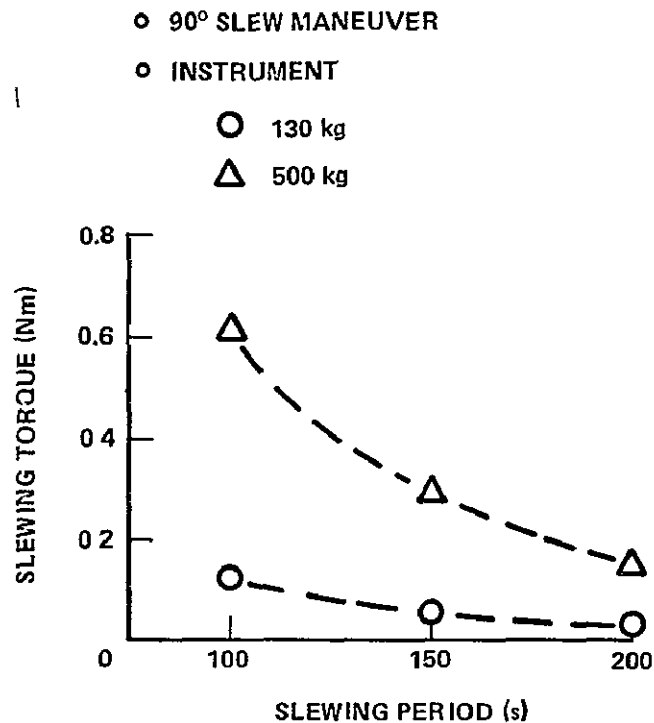


Figure 14. Rigid end mount slewing analysis.

to the soft isolators when performing large slew maneuvers. The comparison also shows the advantage of caging the MPM isolators before making large slew maneuvers.

For comparison, the slewing capabilities were calculated for a rigid end mount and a rigid c.g. mount and are shown in Figures 15 and 16, respectively. Although the c.g. mount is faster than the end mount, the difference in slewing capability should not be significant in most cases.

Tracking

The tracking of an Earth surface target was simulated for both the small and large instruments. Figure 17 shows a summary of MPM tracking performance peak control torque. High and low altitude tracking profiles directly over the target were simulated with a maximum tracking rate of 1.0 degree/s for approximately 470 km altitude and 1.5 degree/s for approximately 310 km

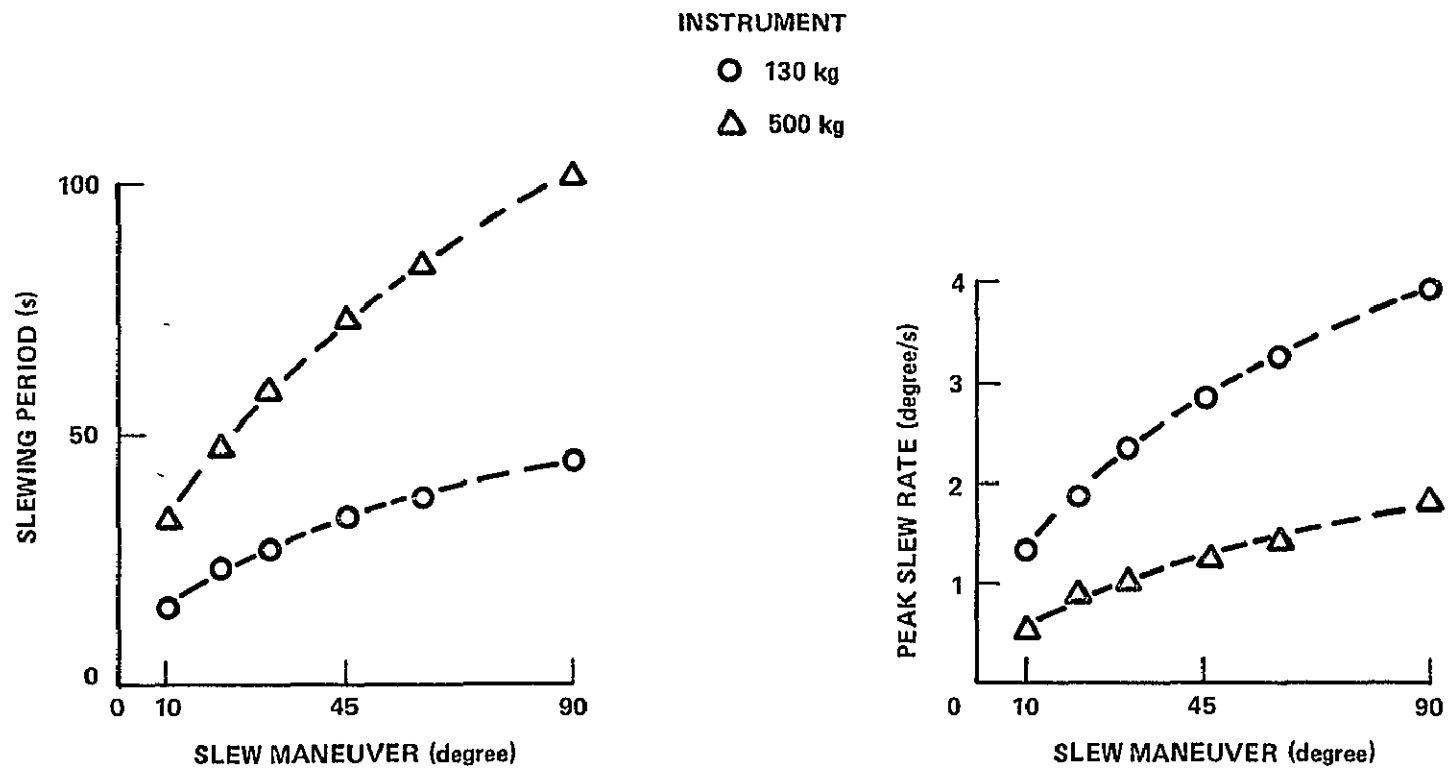


Figure 15. Rigid end mount slewing capability for 0.6 Nm torque limit.

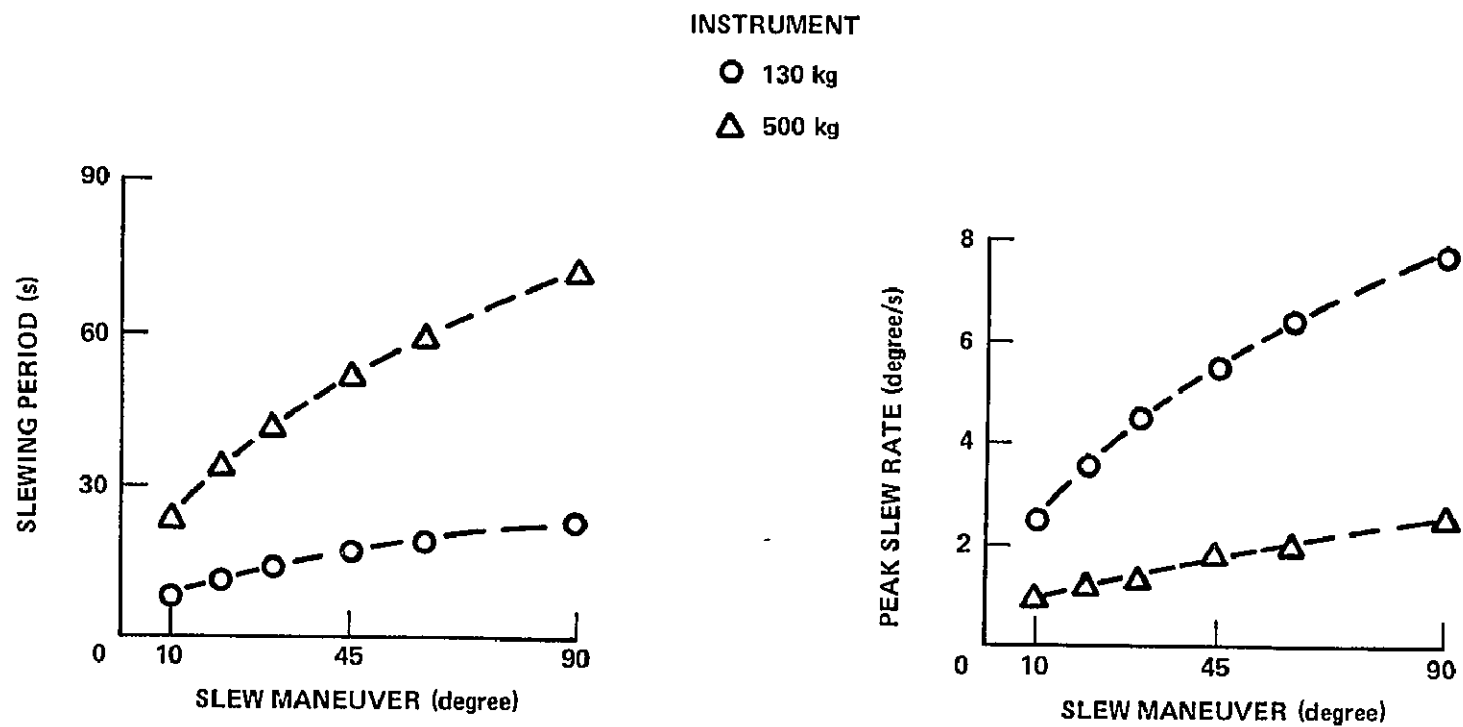


Figure 16. Rigid c.g. mount slewing capability for 0.6 Nm torque limit.

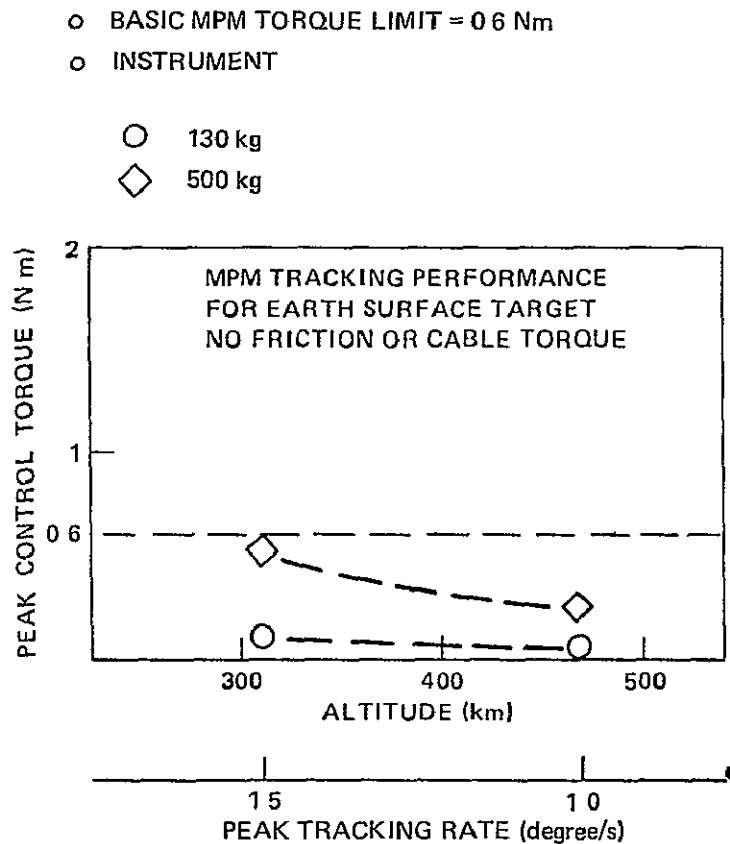
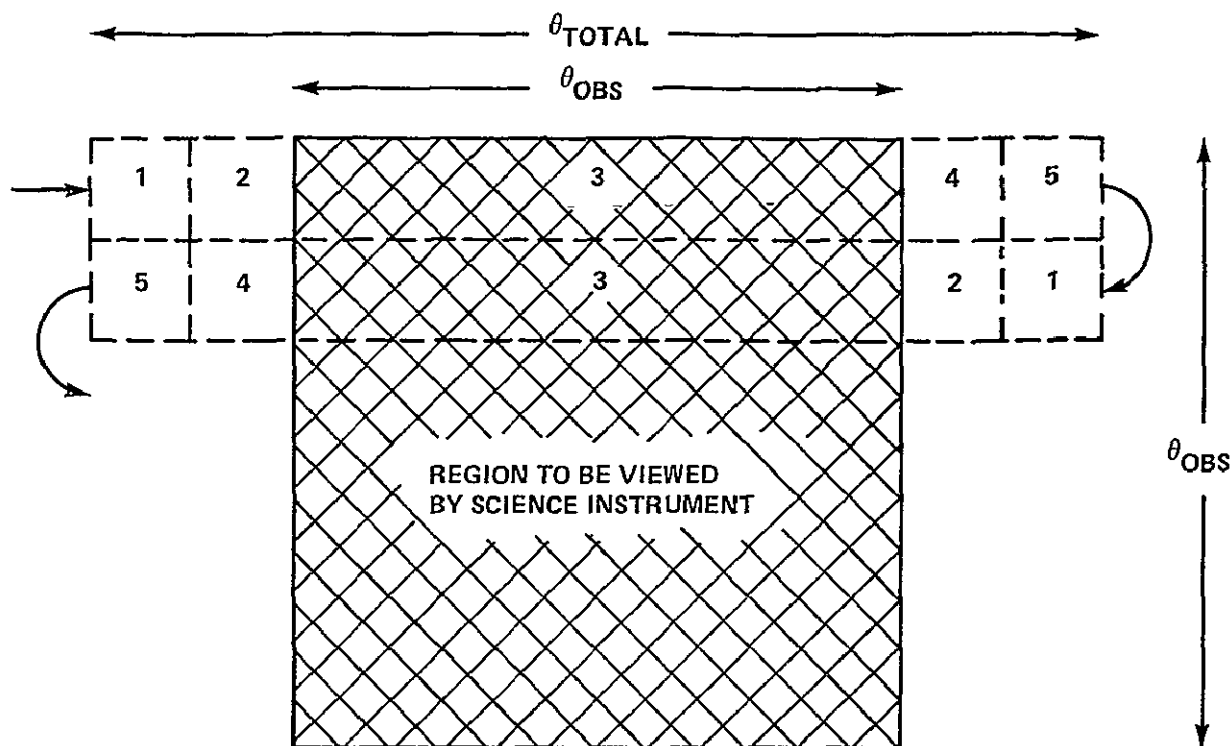


Figure 17. MPM tracking performance.

altitude, respectively. The peak torque is within the basic MPM torque capability of 0.6 Nm for altitudes above 300 km. The dynamic time response plots of MPM tracking performance can be found in Appendix C of Reference 3.

RASTERING PERFORMANCE

Scanning the line of sight of an instrument back and forth across a small region such as an area of the solar disk or a stellar target while the instrument takes data is known as rastering. A typical rastering operation is depicted in Figure 18. The MPM rastering performance is given for typical instrument characteristics and nominal raster parameters which were extracted from Reference 4. A summary of nominal MPM and instrument characteristics for _ _



SEGMENTS OF RASTER SCAN PROFILE

- 1 SCAN RATE IS BUILDING UP
- 2 SCAN RATE IS CONSTANT AND TRACKING ERROR $\geq \theta_{ELIM}$ BUT SETTLING OUT
- 3 SCAN RATE IS CONSTANT AND TRACKING ERROR $< \theta_{ELIM}$ (SCIENCE INSTRUMENT TAKES DATA)
- 4 SCAN RATE IS CONSTANT AND TRACKING ERROR $< \theta_{ELIM}$ (THIS IS OVERSHOOT NECESSARY TO ALLOW FOR SETTLING TIME IN NEXT SCAN LINE)
- 5 SCAN RATE IS DECREASING TO ZERO

Figure 18. Raster scanning a region.

rastering is given in Table 3. MPM and Shuttle/pallet mass characteristics are the same as given in Table 1. A summary of the nominal raster parameters is given in Table 4 for solar physics instrument rastering. MPM rastering performance is also given for parameter variations such as scan rate, pointing position, isolator stiffness, and pedestal height.

The MPM planar simulation was commanded with position and rate commands to simulate raster scanning back and forth across an observation region as illustrated in Figure 18. The position and rate command functions are

TABLE 3. MPM AND INSTRUMENT CHARACTERISTICS
FOR RASTERING

MPM	
Shockmount Stiffness (N/m)	100
Control Loop Bandwidth (Hz)	5
Pointing Position (degree)	90
Control Law: Position and Rate Feedback	
Command Signals: Position and Rate	
Sensor: Perfect Guider	
Instrument	
Mass (kg)	250
Inertia (kg m ²)	150
c.m. Offset (m)	1.24

TABLE 4. NOMINAL RASTERING REQUIREMENTS

Raster Size (arc min)	60 × 60	15 × 15	5 × 5	1.5 × 1.5
Approximate Time per Raster (s)	900	124	56	20
Scan Line Separation (arc s)	30	20	10	5
Number of Scan Lines	120	45	30	18
Scan Rate (arc s/s)	480	320	160	80
Scan Accuracy (arc s) (Over 90% of Raster Duration and 90% of each Scan Line)	10	6.7	3.3	1.7

depicted in Figure 19 as well as the acceleration profile used to derive the command signals. Figure 19 also shows a phase plane representation of the command functions. The phase plane clearly illustrates the observation region being scanned at a constant rate and the overshoot beyond the observation region required to change the scanning direction.

The summary of the simulated MPM rastering performance shown in Table 5 corresponds to the rastering requirements in Table 4. The simulated performance gives the total raster size and time per raster which includes the position overshoot beyond the observation region. The approximate time per raster given in Table 4 was based on the observation raster size, the line scan rate, and the number of scan lines and did not consider position overshoot. The observation duration is presented as a percentage of the total time per raster.

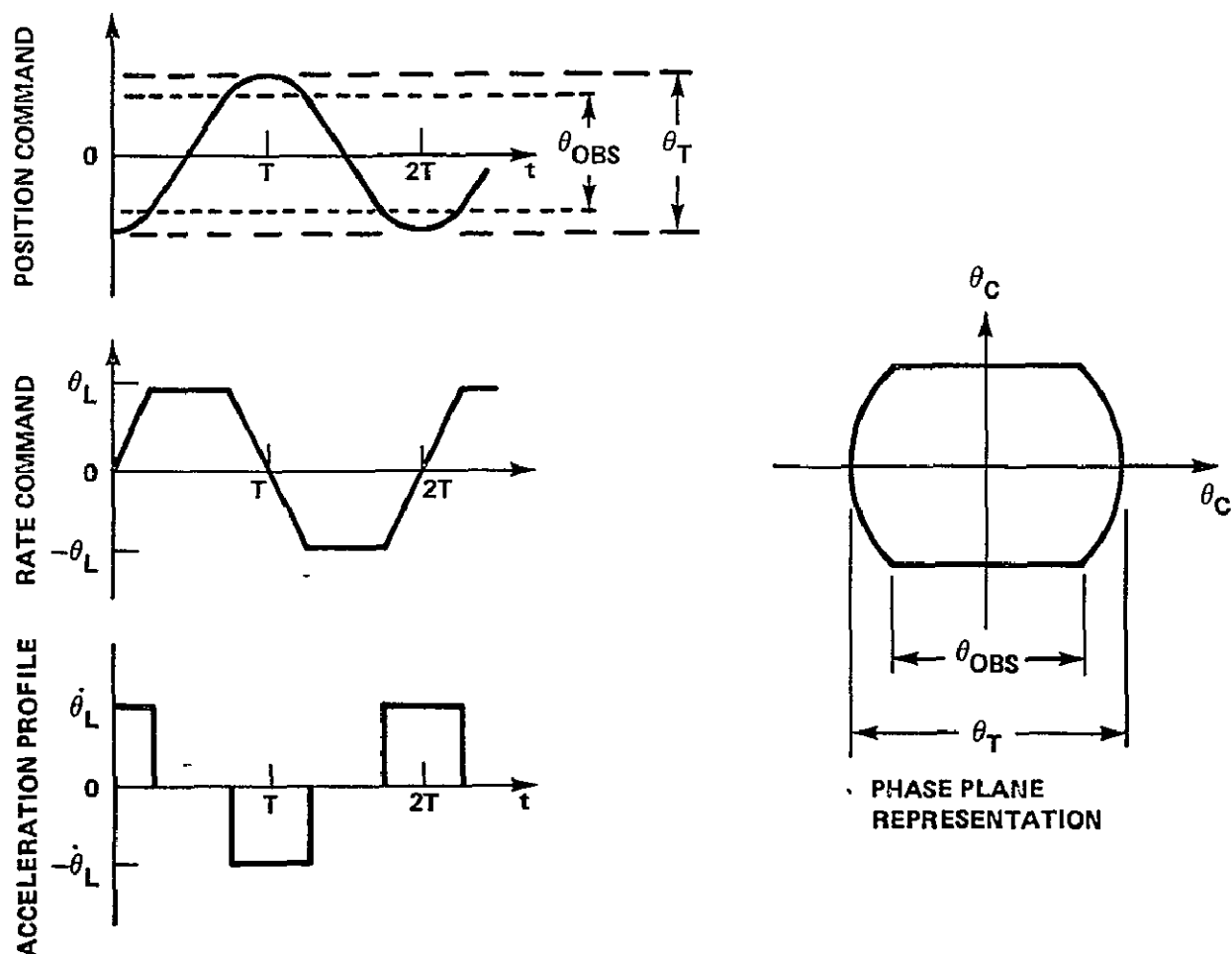


Figure 19. Raster scan command profile.

TABLE 5. MPM RASTERING PERFORMANCE

Raster Size (mm) (Total)	67 × 60	17 × 15	5.4 × 5	1.6 × 1.5
Total Time per Raster (s)	998	151.2	64.4	22.7
Observation Duration (%)	90	82	87	88
Scan Line Separation (arc s)	30	20	10	5
Number of Lines	120	45	30	18
Scan Rate (arc s/s)	480	320	160	80
Scan Accuracy (arc s) (Percentage of each Scan Line)	<1 (100)	<1 (100)	<1 (100)	<1 (100)

The peak scan error was less than 1 arc s which occurred during the overshoot of the observation region; therefore, the scan accuracy requirement was satisfied over 100 percent of each scan line. An ideal guide sensor was assumed. However, ideal raster command signals could be generated with the control computer, provided a calibration sensor and/or another information source were available to supply the initial calibration and raster starting position.

A derivation of a minimum time raster scan based on a given raster size and acceleration limit is presented in Appendix B. To minimize the total time per raster, the observation duration should be 50 percent. Faster scan rates could be used for all rasters listed in Table 4 to reduce the total time per raster. The total time per raster for several scan rates is given in Figure 20 for the 90 arc s raster. Using the derivation in Appendix B, a scan rate of 230 arc s/s would result in a minimum total time per raster of approximately 14.1 s compared with the nominal line scan rate of 80 arc s/s, resulting in a total time per raster of approximately 22.7 s. Figure 20 also shows the peak control torque as a function of scan rate for 45 and 90 degree pointing positions. The 90 degree pointing position is along the Shuttle Z-axis that is perpendicular to the payload bay and the 45 degree pointing position is relative to the payload bay and looking forward as illustrated in Figure 1. Figure 20 shows MPM rastering performance to be essentially insensitive to variations in scan rate and pointing position for the 90 arc s raster. This is a significant point since a simplified dynamic analysis by the Jet Propulsion Laboratory [5] had predicted the end

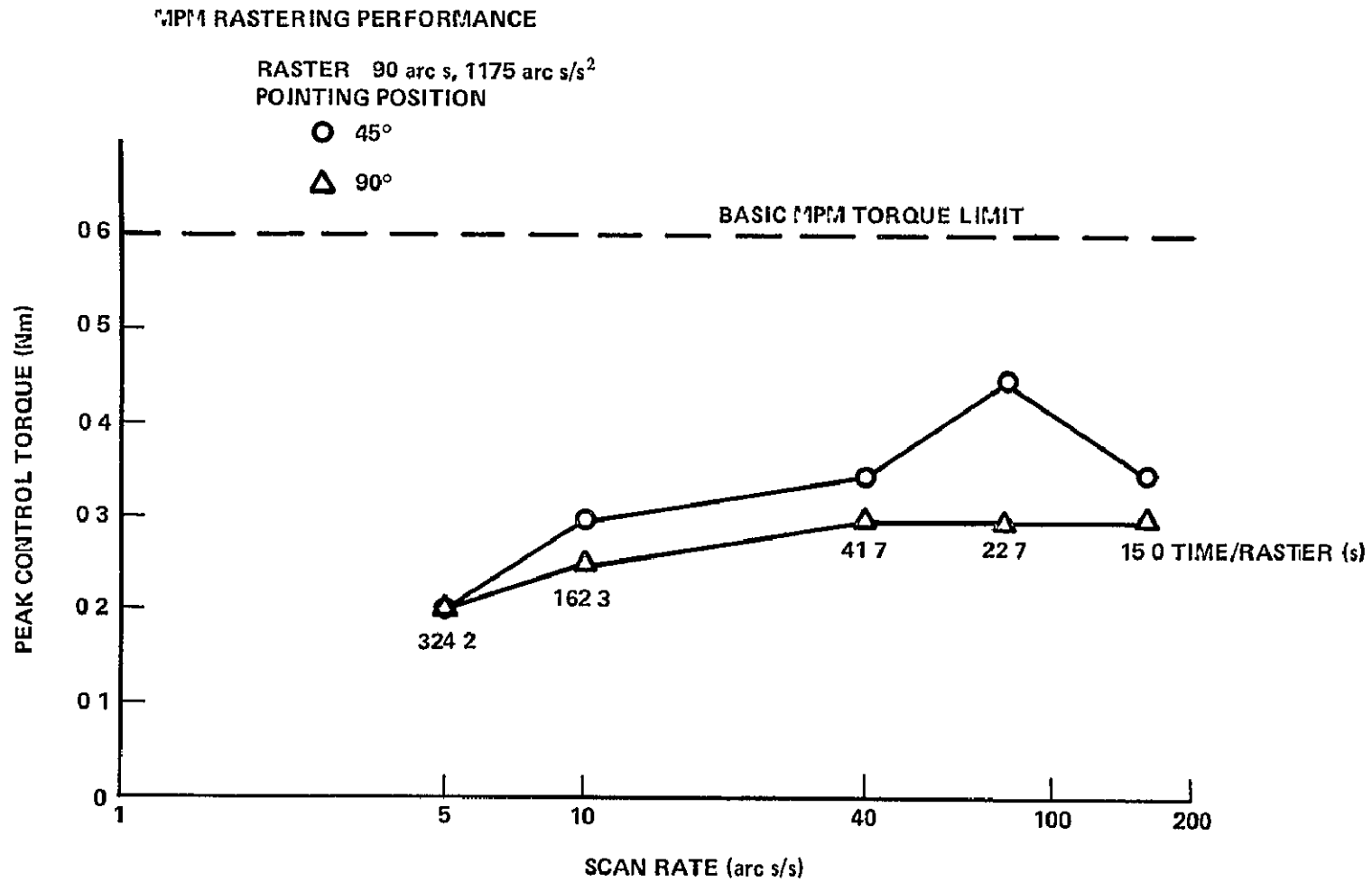


Figure 20. MPM rastering torque versus scan rate for the 90 arc s raster.

mounted pointing system to be sensitive to scan frequency as shown in Figure 21. Also, the simulation analysis which follows has shown that with the proper selection of MPM parameters, the control torque can be much less than for a c.g. mount.

The shockmount stiffness was varied over a wide range to study the effect on MPM rastering performance. Figure 22 shows the performance for the 90 arc s raster and Figure 23 gives the performance for the 3600 arc s raster. For the 90 arc s raster, a shockmount stiffness up to 1000 N/m could be used with a satisfactory margin from the resonant peak. However, Figure 23 shows the nominal shockmount stiffness of 100 N/m to be unsatisfactory for the 3600 arc s raster, and a reduction to approximately 50 N/m stiffness is needed to achieve satisfactory performance. Figures 22 and 23 show the surprising effect of gimbal forces acting on the instrument during rastering to reduce the control torque below a level required for a c.g. mount. This observation of reduced control torque when using a soft-mounted pointing system such as the MPM has been studied and verified on several independent computer simulations.

The effect on control torque of varying the pedestal height is shown in Figure 24. Pedestal heights up to approximately 0.5 m reduce the peak control torque, and at approximately 0.1 m the peak control torque is equivalent to that of a c.g. mount.

A typical MPM rastering dynamics response plot is shown in Figure 25. This illustration is for the 90 arc s raster, a scan rate of 80 arc s/s, and is based on an acceleration limit of 1175 arc s/s². The peak values of control torque are slightly less than 0.3 Nm, and the corresponding peak values of tracking error are slightly less than 0.6 arc s. Because the same control law gains were used for all rastering runs, the relationship between tracking error and control torque is consistent throughout the section on rastering performance. The peak magnitudes of tracking error in arc seconds are approximately twice the peak magnitudes of control torque in Newton-meters.

The changing of scan lines is illustrated in Figure 18 by stepping from segment 5 to segment 1 of the raster scan profile. A smooth transition between scan lines can be made using position and rate command signals based on an acceleration limit profile as depicted in Figure 26. The changing of scan lines occurs during the overshoot of the observation region. A typical MPM dynamic response to a 5 arc s scan line step command is shown in Figure 27.

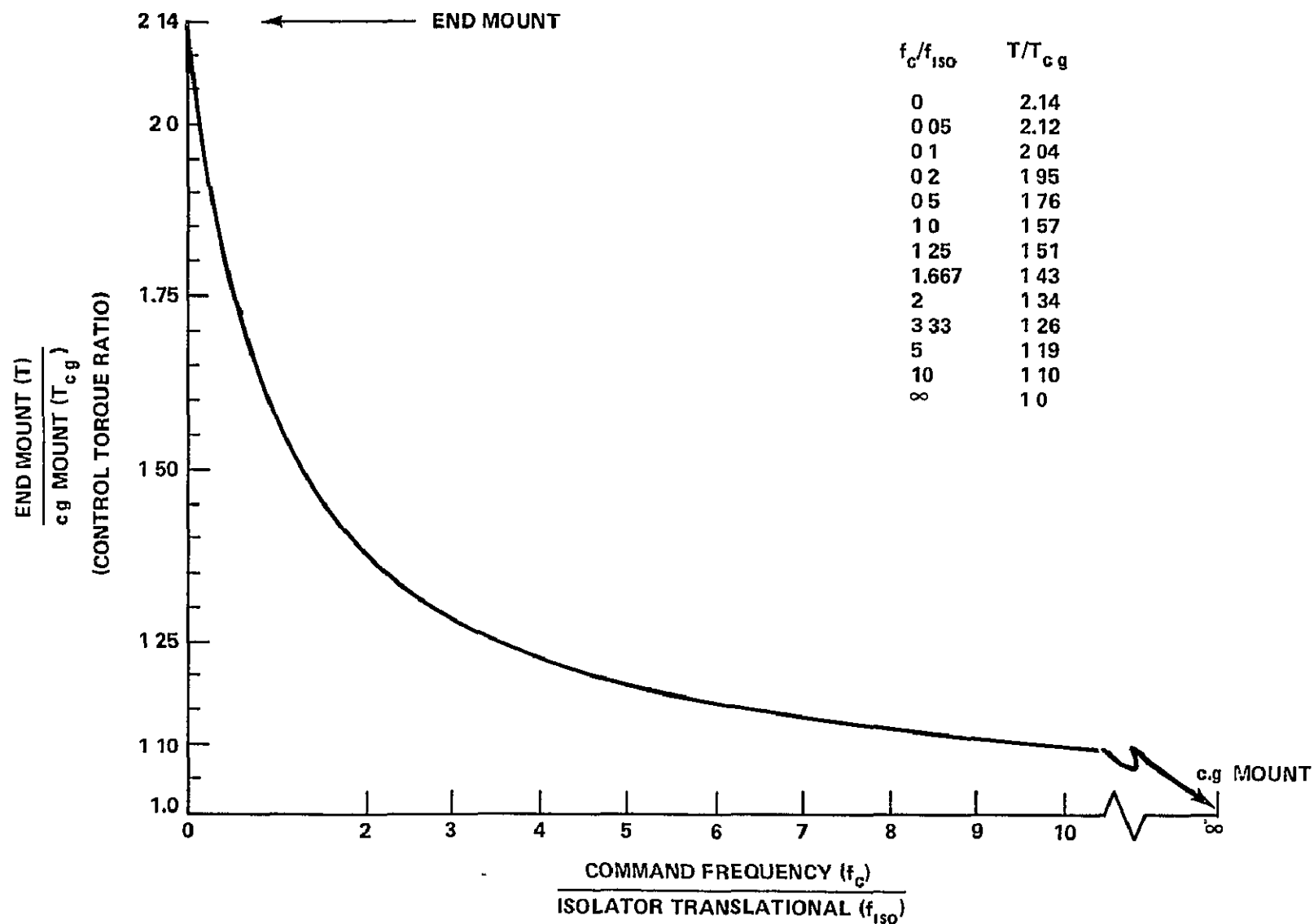


Figure 21. End mount/c.g. mount control torque ratio for a simplified end mount model.

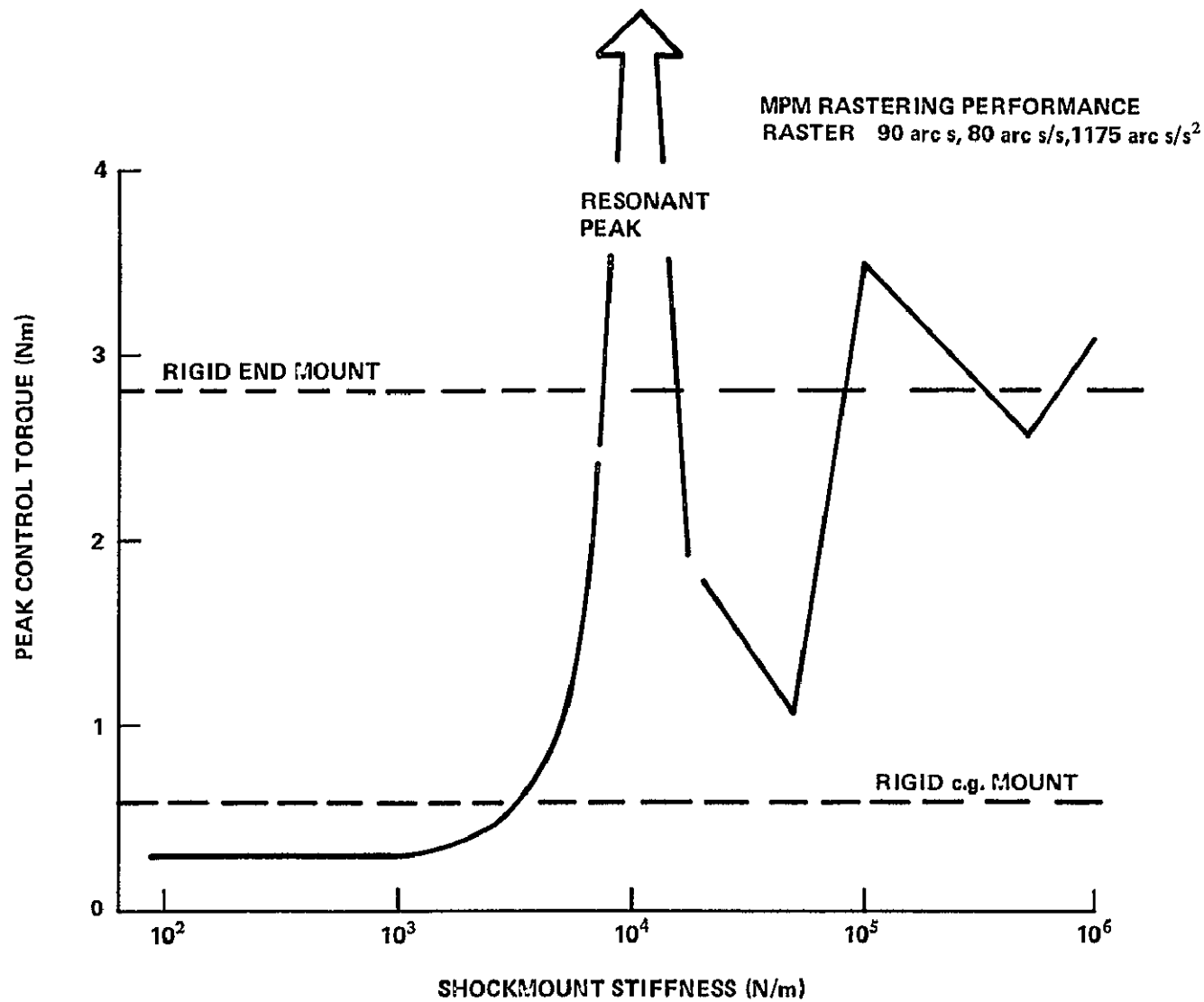


Figure 22. MPM rastering torque versus shockmount stiffness for the 90 arc s raster.

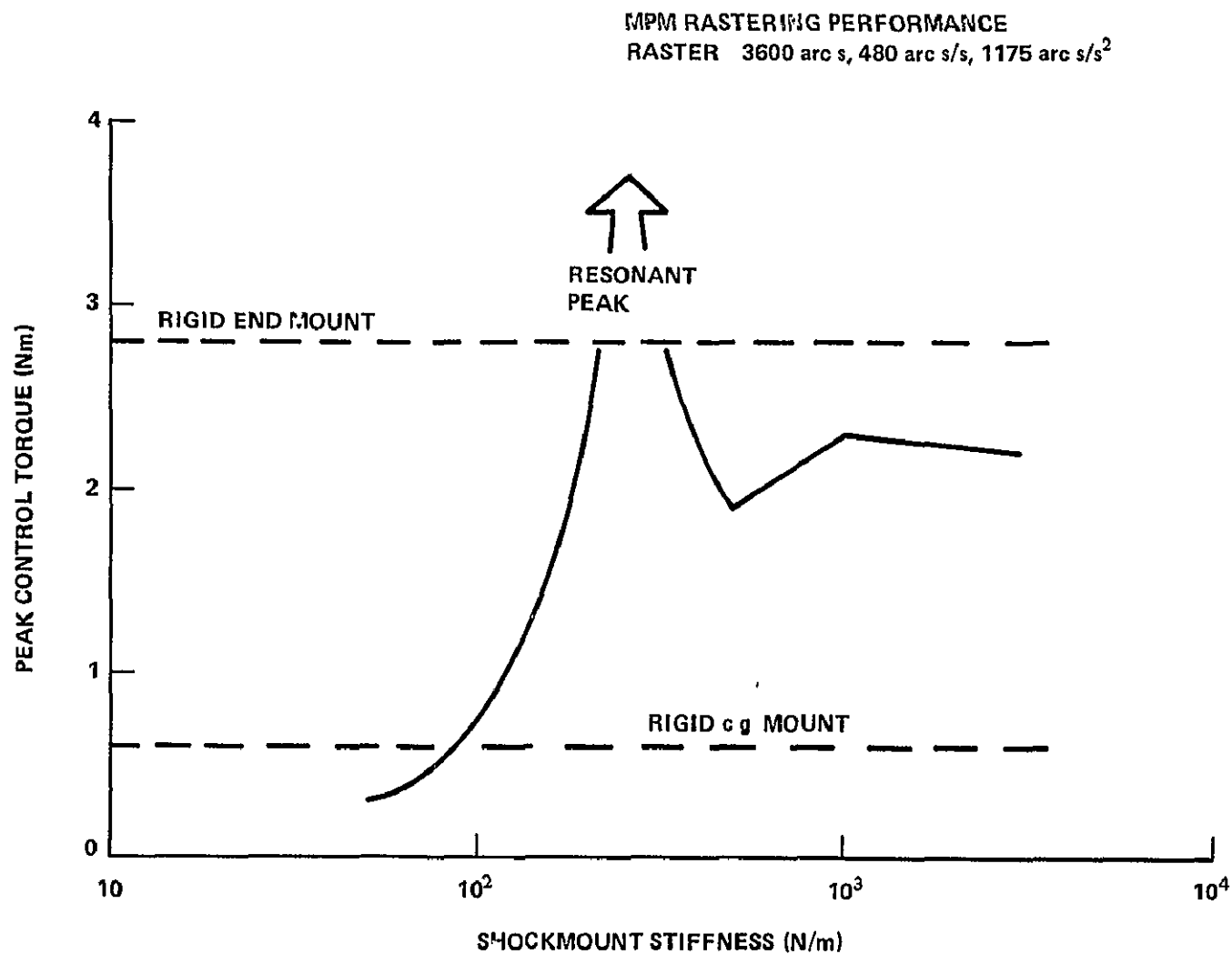


Figure 23. MPM rastering torque versus shockmount stiffness for the 3600 arc s raster.

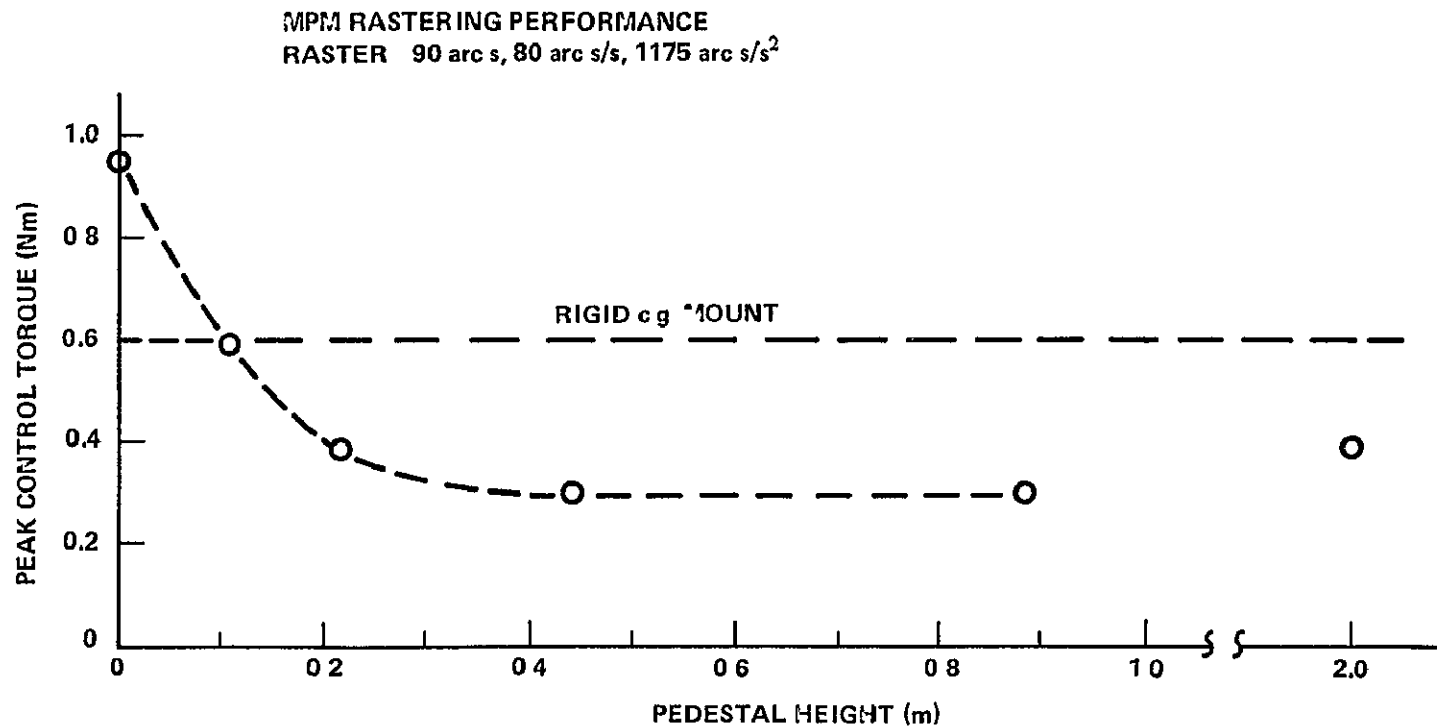


Figure 24. MPM rastering torque versus pedestal height for the 90 arc s raster.

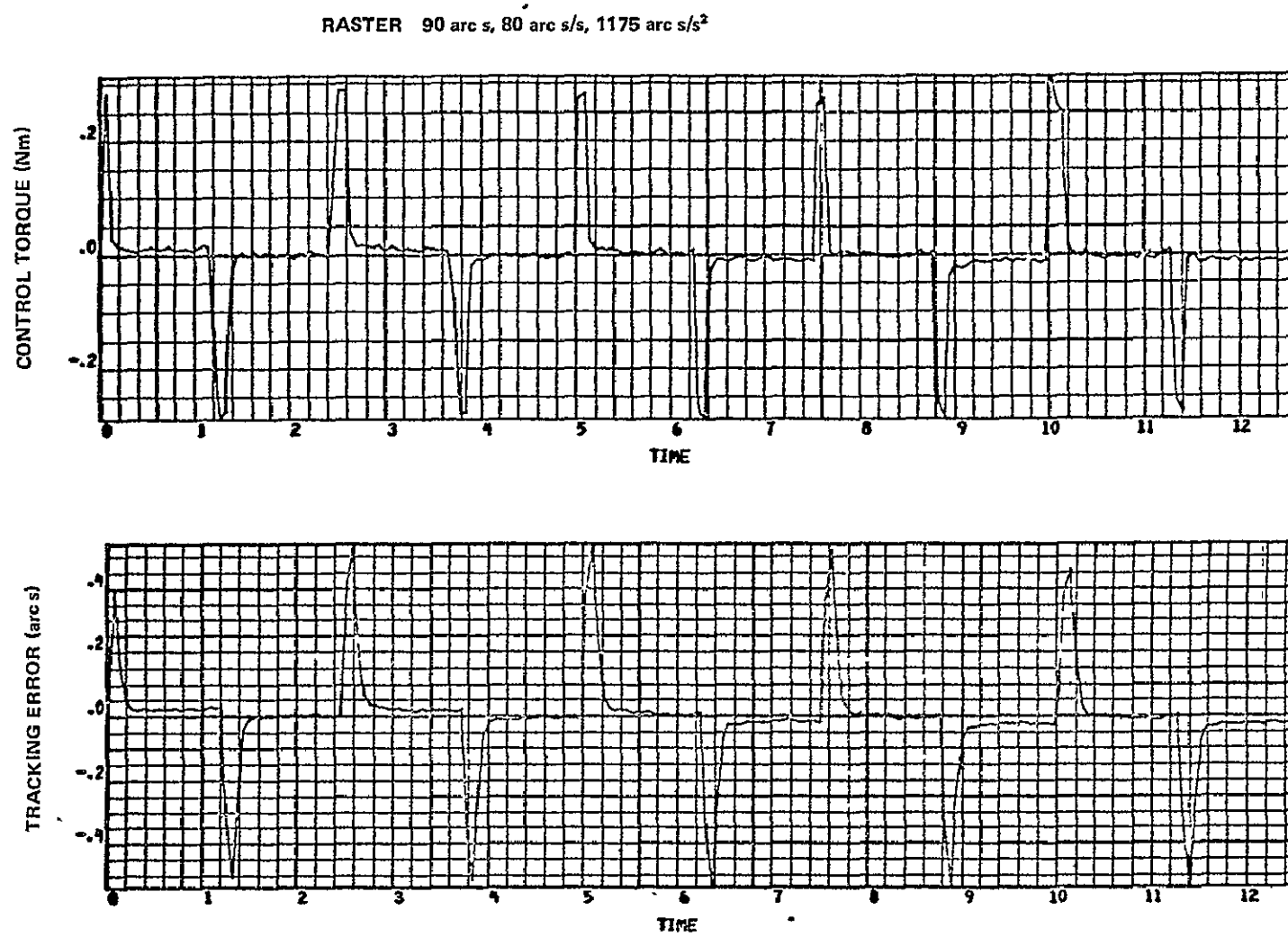


Figure 25. Typical rastering dynamic response.

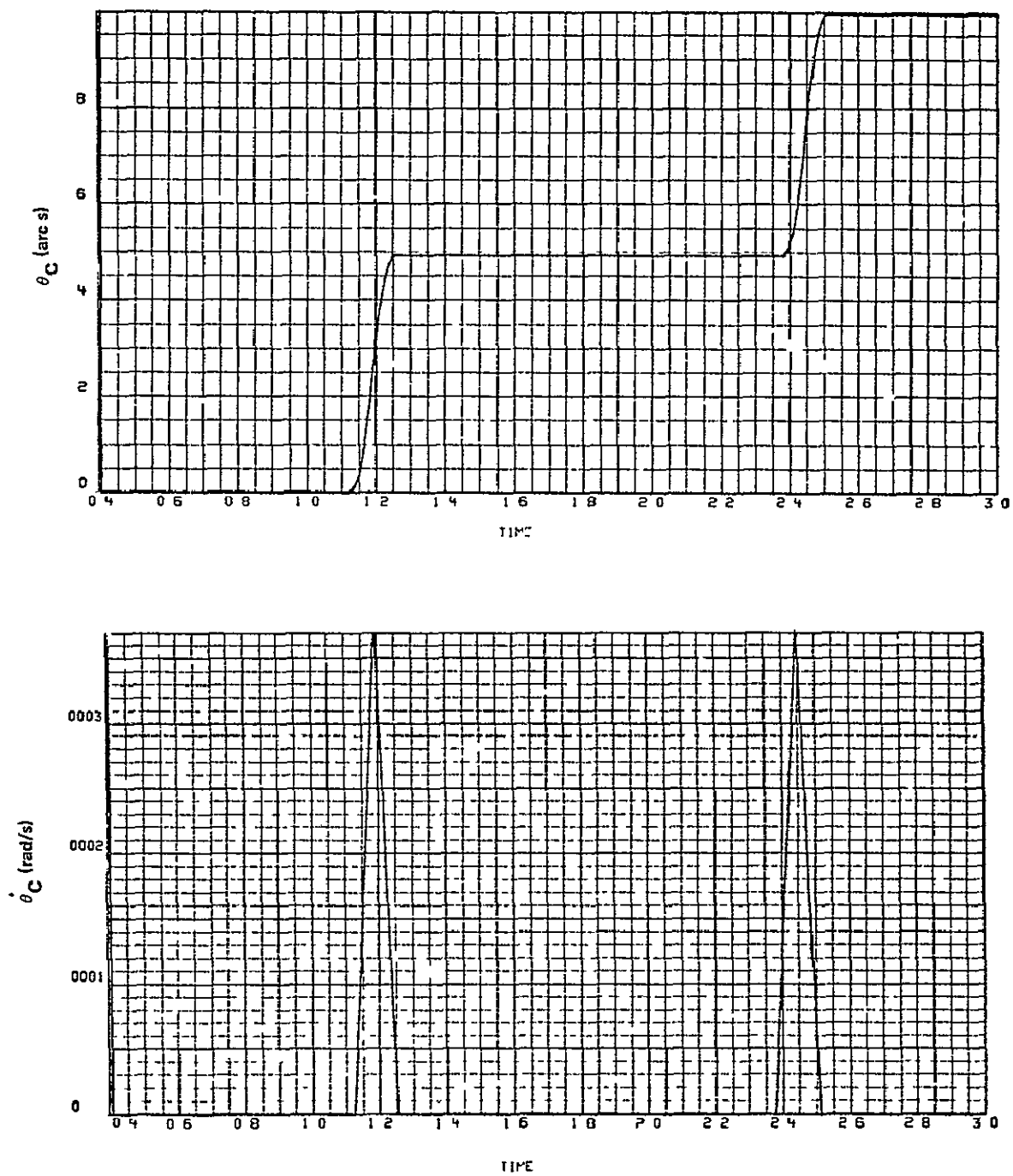


Figure 26. Scan line transition command profile.

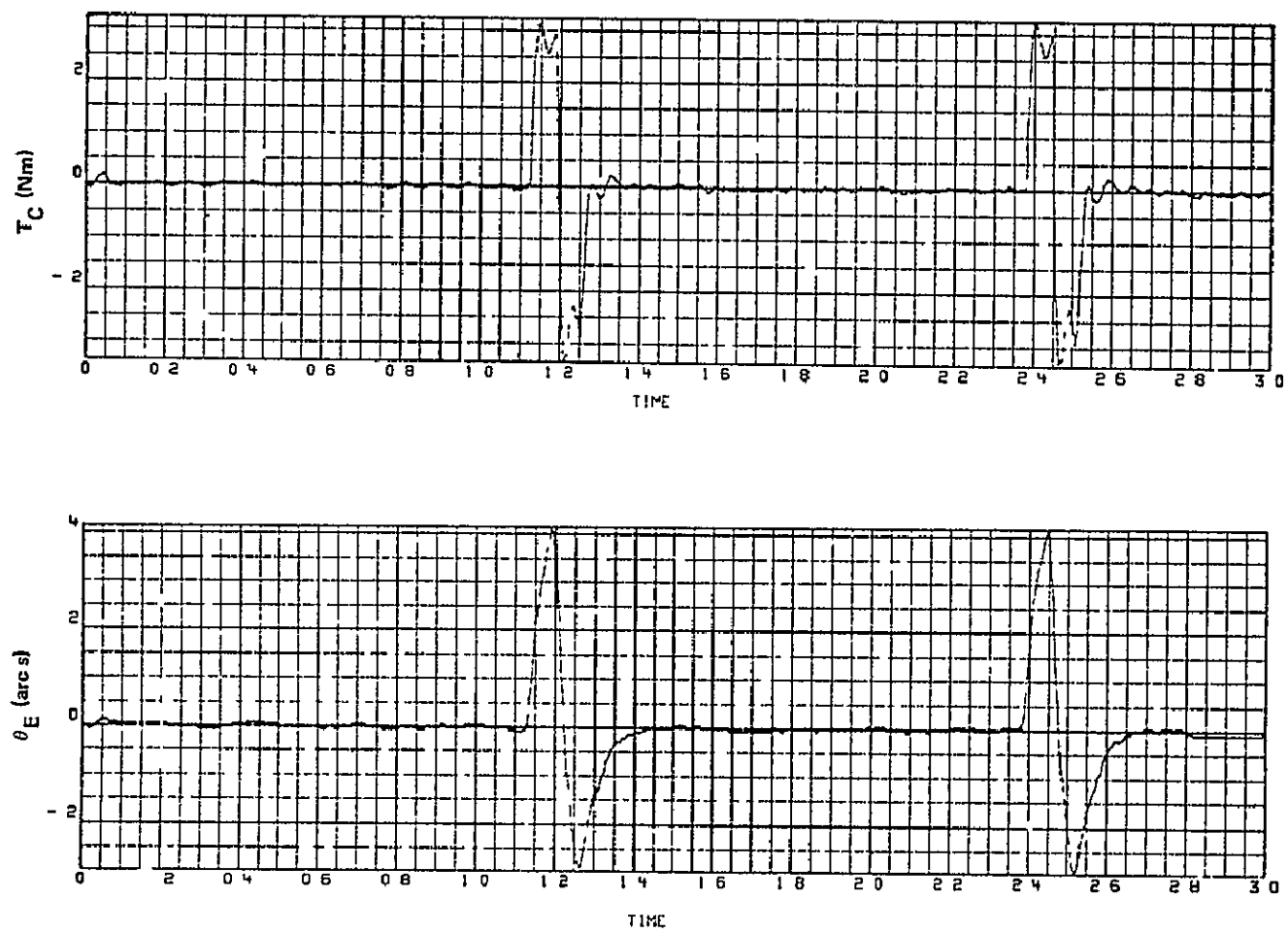


Figure 27. Typical MPM response to scan line transition.

CONCLUSION

The MPM can meet the pointing requirements of typical small instruments, such as for Spacelab and OFT missions. Satisfactory performance can be achieved in all pointing requirement areas including inertial pointing, slewing, tracking, and rastering with very few restrictions.

Excellent inertial pointing performance was achieved for the small and large instruments over a nominal pointing position range, i.e., 40 to 90 degrees. The peak stability error decreased with the square of the control bandwidth increase while the peak control torque was the same for all control frequencies. The large instrument had considerably less peak stability error than the small instrument with only a slightly higher control torque required. The larger instruments appear to effect greater disturbance isolation than do small instruments. Larger payloads limited only by the pallet capability could be inertially pointed by the MPM.

Slewing between targets was demonstrated for a soft and hard mounted MPM and a c.g. mount with the same torque limit. The peak control torque required for slewing with the hard mounted MPM was approximately one-third that required for the soft mounted MPM. Therefore, the MPM isolators should be caged when making large slew maneuvers. The c.g. mount can slew faster than the end mount, however, the difference in slewing capability should be insignificant in most cases.

The capability to track directly over an Earth surface target was demonstrated for altitudes above 300 km for both the small and large instruments. The peak tracking error was less than 1 arc s based on a perfect guide sensor. Earth surface target tracking may require stiffer shockmount isolators than for inertial pointing or rastering to prevent excessive pedestal motion. Coarse tracking may be accomplished with the isolators caged.

Excellent MPM rastering performance was demonstrated with a typical solar physics instrument and for typical rastering requirements. A parametric study via computer simulation showed the MPM control torque to be less sensitive to raster scan rate than had been anticipated. However, a sensitivity to shockmount stiffness was discovered and analyzed. The proper selection of shockmount stiffness and pedestal height can result in a smaller control torque

than for a c.g. mount. The changing of scan lines required less time than the overshoot of the observation region and presents no apparent problem. Due to the impact of pedestal and shockmount characteristics on the rastering dynamics, rastering appears to be a design driver for the soft shockmount isolators and the pedestal.

APPENDIX A

SIMULATION MATH MODEL

The equations of motion are presented for a planar model of the three-body configuration shown in Figure 1 of the text. The three bodies are the Shuttle, the pedestal, and the instrument. The motion is restricted to the X-Z plane; therefore, each body can translate in the X and Z directions and rotate about the Y-axis.

Since the pedestal was relatively small compared to the instrument, the math model can be simplified by assuming the pedestal to be a massless link between the gimbal point and the soft spring isolators. This assumption has been satisfactorily verified by comparing the results of this model with results from complex detailed models which require more time and larger computers for simulation.

The equations of motion were linearized about the command angle, θ_C , assuming the command angle to be constant during an observation and the angular error of the instrument to be small. The angular motion of the Shuttle and the pedestal were also assumed to be small.

The translational equations of the instrument and the Shuttle are as follows:

$$\begin{aligned}
 M_1 \ddot{X}_1 + K_T (X_1 - X_S + R_1 (1 - \cos \theta_C - \theta_E \sin \theta_C) + R_2 \theta_2) \\
 + D_T (\dot{X}_1 - \dot{X}_S + R_1 \dot{\theta}_1 \sin \theta_C + R_2 \dot{\theta}_2) \simeq 0
 \end{aligned}
 \tag{A-1}$$

$$\begin{aligned}
 M_1 \ddot{Z}_1 + K_T (Z_1 - Z_S + R_1 (\sin \theta_C - \theta_E \cos \theta_C) - R_3 \theta_3) \\
 + D_T (\dot{Z}_1 - \dot{Z}_S + R_1 \dot{\theta}_1 \cos \theta_C - R_3 \dot{\theta}_3) \simeq 0
 \end{aligned}
 \tag{A-2}$$

$$\begin{aligned}
& M_S \ddot{X}_S - K_T (X_1 - X_S + R_1 (1 - \cos \theta_C - \theta_E \sin \theta_C) + R_2 \theta_2) \\
& - D_T (\dot{X}_1 - \dot{X}_S + R_1 \dot{\theta}_1 \sin \theta_C + R_2 \dot{\theta}_2) \simeq F_{MX}
\end{aligned} \tag{A-3}$$

$$\begin{aligned}
& M_S \ddot{Z}_S - K_T (Z_1 - Z_S + R_1 (\sin \theta_C - \theta_E \cos \theta_C) - R_3 \theta_S) \\
& - D_T (\dot{Z}_1 - \dot{Z}_S + R_1 \dot{\theta}_1 \cos \theta_C - R_3 \dot{\theta}_S) \simeq F_{MZ}
\end{aligned} \tag{A-4}$$

The rotational equation of the instrument, the Shuttle, and the pedestal are as follows:

$$\begin{aligned}
& I_1 \ddot{\theta}_1 + K_T [R_1 \sin \theta_C (X_1 - X_S + R_1 (1 - \cos \theta_C - \theta_E \sin \theta_C) + R_2 \theta_2) \\
& + R_1 \cos \theta_C (Z_1 - Z_S + R_1 (\sin \theta_C - \theta_E \cos \theta_C) - R_3 \theta_S)] \\
& + D_T [R_1 \sin \theta_C (\dot{X}_1 - \dot{X}_S + R_1 \dot{\theta}_1 \sin \theta_C + R_2 \dot{\theta}_2) \\
& + R_1 \cos \theta_C (\dot{Z}_1 - \dot{Z}_S + R_1 \dot{\theta}_1 \cos \theta_C - R_3 \dot{\theta}_S)] \simeq T_C
\end{aligned} \tag{A-5}$$

$$\begin{aligned}
& I_S \ddot{\theta}_S - K_T [R_3 (Z_1 - Z_S + R_1 (\sin \theta_C - \theta_E \cos \theta_C) - R_3 \theta_S)] \\
& - K_R (\theta_2 - \theta_S) - D_T [R_3 (\dot{Z}_1 - \dot{Z}_S + R_1 \dot{\theta}_1 \cos \theta_C - R_3 \dot{\theta}_S)] \\
& - D_R (\dot{\theta}_2 - \dot{\theta}_S) \simeq -R_M^F F_{MZ}
\end{aligned} \tag{A-6}$$

$$\begin{aligned}
& K_T [R_2 (\dot{X}_1 - \dot{X}_S + R_1 (1 - \cos \theta_C - \theta_E \sin \theta_C) + R_2 \dot{\theta}_2)] \\
& + K_R (\theta_2 - \theta_S) + D_T [R_2 (\dot{X}_1 - \dot{X}_S + R_1 \dot{\theta}_1 \sin \theta_C + R_2 \dot{\theta}_2)] \\
& + D_R (\dot{\theta}_2 - \dot{\theta}_S) \approx -T_C
\end{aligned} \tag{A-7}$$

where

$$\theta_E = \theta_C - \theta_1 \tag{A-8}$$

$$T_C = K_P \theta_E - K_1 \dot{\theta}_1 + K_I \int \theta_E dt \quad . \tag{A-9}$$

The instrument line of sight error (θ_E) was defined as the difference between the commanded attitude (θ_C) and the actual instrument attitude (θ_1). The instrument control torque was derived from a simple proportional plus rate control law with an option of including integral control.

For large maneuvers such as slewing from one target to another, the command angle is no longer constant. Therefore, the previously mentioned equations of motion are nonlinear during slewing.

APPENDIX B

MINIMUM TIME RASTER SCAN

The minimum time per scan line is derived based on a given size raster and acceleration limit. The raster size is dictated by the experiment requirements. The acceleration limit must be selected so as to operate within the torque capability of the pointing system.

Figure B-1 shows the rastering rate command profile where the settling time is assumed to be negligible. The total time per scan line is

$$T = \frac{2\dot{\theta}_L}{\ddot{\theta}_L} + \frac{\theta_{OBS}}{\dot{\theta}_L}$$

where

θ_{OBS} = the observation or data taking segment of the scan line

$\dot{\theta}_L$ = the scan rate command limit

$\ddot{\theta}_L$ = the acceleration limit used to determine the slope of the rate command profile.

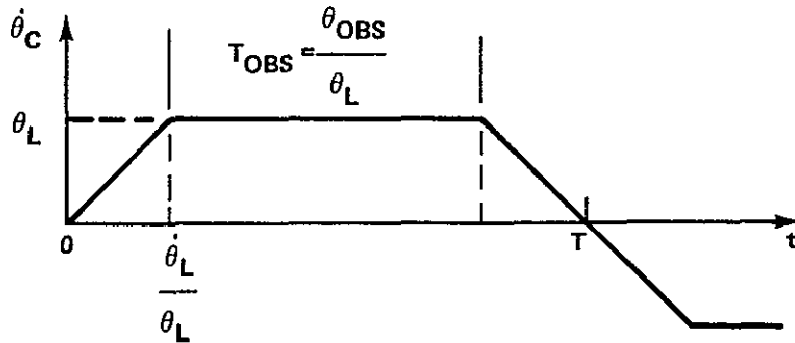


Figure B-1. Rastering rate command profile where settling time is assumed negligible.

The condition for minimum total time with respect to $\dot{\theta}_L$ is

$$\frac{\partial T}{\partial \dot{\theta}_L} = \frac{2}{\dot{\theta}_L} - \frac{\theta_{OBS}}{\dot{\theta}_L^2} = 0$$

or

$$2\dot{\theta}_L^2 = \theta_{OBS} \ddot{\theta}_L \quad .$$

Defining the ratio of observation time per scan line (T_{OBS}) to total time as

$$R = \frac{T_{OBS}}{T} \quad ,$$

then

$$R = \frac{\frac{\theta_{OBS}}{\dot{\theta}_L}}{\frac{2\dot{\theta}_L}{\ddot{\theta}_L} + \frac{\theta_{OBS}}{\dot{\theta}_L}} = \frac{1}{1 + \frac{2\dot{\theta}_L^2}{\theta_{OBS} \ddot{\theta}_L}} \quad .$$

Using the condition for minimum total time, i. e., $2\dot{\theta}_L^2 = \theta_{OBS} \ddot{\theta}_L$ then

$$R = \frac{1}{1 + \frac{\theta_{OBS} \ddot{\theta}_L}{\theta_{OBS} \ddot{\theta}_L}} = \frac{1}{2} \quad .$$

Therefore, the minimum time per scan line is twice the observation time, i.e.,

$$T_{\text{MIN}} = 2T_{\text{OBS}}$$

where the scan rate command limit is defined as

$$2\ddot{\theta}_L = \theta_{\text{OBS}} \ddot{\theta}_L \quad .$$

Determining the total time per scan line (T) in terms of the ratio R gives

$$T = \sqrt{\frac{2\theta_{\text{OBS}}}{\ddot{\theta}_L R(1 - R)}} = K \sqrt{\frac{2}{R(1 - R)}}$$

where

$$K = \sqrt{\frac{\theta_{\text{OBS}}}{\ddot{\theta}_L}}$$

is a constant. Therefore,

$$\frac{T}{K} = \sqrt{\frac{2}{R(1 - R)}}$$

which yields Figure B-2. Figure B-2 illustrates the minimum time per scan line being twice the observation time.

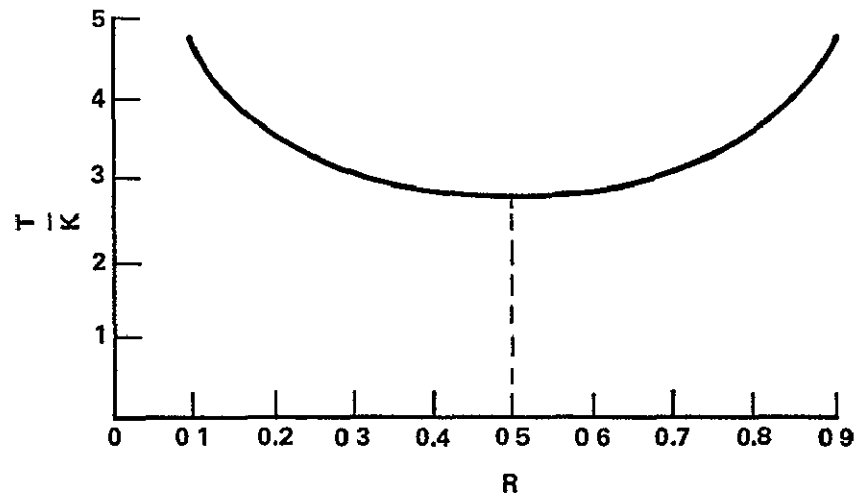


Figure B-2. Minimum time per scan line at twice the observation time.

The derivation is based on a scan rate command limit to minimized time. The experiment data taking capability may or may not allow such a scan rate.

REFERENCES

1. Nein, M. E. and Nicaise, P. D.: An Assessment of the Instrument Pointing Subsystem (IPS) Requirements for Spacelab Missions. NASA TM X-64896, November 1974.
2. Fritz, C. G.; Howell, J. T.; Nicaise, P. D.; and Parker, J. R.. A Miniaturized Pointing Mount for Spacelab Missions. NASA TM X-64972, November 25, 1975.
3. Conway, B. A. and Hendricks, T. C.: A Summary of the Skylab Crew/Vehicle Disturbances Experiment T-013. NASA TN D-8128, March 1976.
4. Nein, M. E. and Nicaise, P. D.: Experiment Pointing Subsystems (EPS) Requirements for Spacelab Missions. NASA TM X-64978, December 1975.
5. Russ, Kenneth M.: EPM Technical Information. Jet Propulsion Laboratory, April 22, 1976.

BIBLIOGRAPHY

- Marmann, R. A.: Feasibility of Raster Scanning a Solar Telescope with the Spacelab Instrument Pointing System (IPS). NASA/MSFC EL51(278-75), November 13, 1975.


APPROVAL

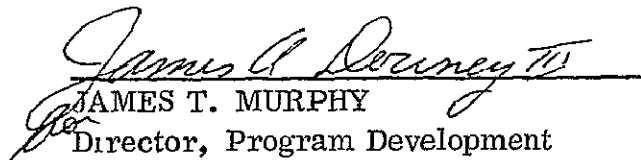
MINIATURIZED POINTING MOUNT
PERFORMANCE ANALYSIS

By Joe T. Howell, Jr.

The information in this report has been reviewed for security classification. Review of any information concerning Department of Defense or Atomic Energy Commission programs has been made by the MSFC Security Classification Officer. This report, in its entirety, has been determined to be unclassified.

This document has also been reviewed and approved for technical accuracy.


CHARLES R. DARWIN
Director, Preliminary Design Office


JAMES T. MURPHY
Director, Program Development

DISTRIBUTION

INTERNAL

DA01

W. R. Lucas

DD01

R. G. Smith

DS30

C. R. O'Dell

EA01

J. E. Kingsbury

EE01

W. R. Marshall

W. Haeussermann

PA01

J. T. Murphy

J. A. Downey

JA01

O. C. Jean

R. Ise

EL01

H. E. Thomason

W. B. Chubb (5)

ED01

J. A. Lovingood

J. C. Blair

S. M. Seltzer (5)

R. L. Lawlence

J. S. Spear

EC01

F. B. Moore

J. L. Mack

P. T. Golley

C. E. Lee

ES01

C. A. Lundquist

NA01

T. J. Lee (5)

PS01

H. P. Gierow

M. E. Nein (5)

PD01

C. R. Darwin

F. E. Digesu

W. K. Fikes

D. N. Schultz

P. D. Nicaise

R. Kozub (30 copies)

J. T. Howell (30)

CC01

L. D. Wofford, Jr.

AS61 (2)

AS61L (8)

AT01

EXTERNAL

National Aeronautics and Space Administration

Washington, D. C. 20546

Attn: P. E. Culbertson, Code O

G. F. Esenwein, Code OR

W. Piotrowski, Code OR

A. E. Timothy, Code ST

N. G. Roman, Code SAA

E. R. Schmerling, Code ST

D. G. McConnell, Code EB

J. W. Haughey, Code MTG

M. A. Calabrese, Code ERF

Harold Glaser, Code ST

Frank Martin, Code SA

W. B. Gevarter, Code RES

A. J. Calio, Code SD

Goddard Space Flight Center

Greenbelt, Maryland 20771

Attn: W. Scull, Code 703.0

D. Leckrone, Code 671.0

W. Neupert, Code 682.0

E. Schmidt, Code 721.2

Ames Research Center

Moffett Field, California 94035

Attn: L. S. Young, Code SDF/244-13

James P. Murphy, Code SDF/244-13

Lyndon B. Johnson Space Center

Houston, Texas 77058

Attn: R. F. Hergert, Code TA

A. C. Holt, Code CG2

K. G. Hemze, Code TE

Jet Propulsion Laboratory

4800 Oak Grove Drive

Pasadena, California 91103

Attn: K. M. Russ, Code 198/112B

E. Mettler, Code 198/112A

Scientific and Technical Information

Facility (25)

P. O. Box 8757

Baltimore/Washington International Airport

Baltimore, Maryland 21240